Building crystalline topological superconductors from Shiba lattices

Martina O. Soldini[1], Felix Küster[2], Glenn Wagner[1], Souvik Das[2], Amal Aldarawsheh[3,5], Ronny Thomale[4,6], Samir Lounis[3,5], Stuart S. P. Parkin[2], Paolo Sessi[2], Titus Neupert[1]

[1] *University of Zurich, Winterthurerstrasse 190, 8057 Zurich, Switzerland,*
[2] *Max Planck Institute of Microstructure Physics, Halle, Germany,*
[3] *Peter Grünberg Institut and Institute for Advanced Simulation, Forschungszentrum Jülich & JARA, Jülich, Germany.*
[4] *Institut fur Theoretische Physik und Astrophysik, Universität Würzburg, Würzburg, Germany.*
[5] *Faculty of Physics, University of Duisburg-Essen and CENIDE, Duisburg, Germany.*
[6] *Department of Physics and Quantum Centers in Diamond and Emerging Materials (QuCenDiEM) Group, Indian Institute of Technology Madras, Chennai, India.*

Localized or propagating Majorana boundary modes are the key feature of topological superconductors. While being a rarity in natural compounds, the tailored manipulation of quantum matter offers novel opportunities for their realization. Specifically, lattices of Shiba bound states that arise when magnetic adatoms are placed on the surface of a conventional superconductor can be used to create topological minibands within the superconducting gap of the substrate. Here, we exploit the possibilities of scanning tunneling microscopy to create and probe adatom lattices with single atom precision to create topological crystalline superconductors. Their topological character and boundary modes are protected by the spatial symmetries of the adatom lattice. We combine scanning probe spectroscopy, spin-sensitive measurements, first principle calculations, and theoretical modeling to to reveal signatures consistent with the realization of two types of mirror-symmetry protected topological superconductors: (i) with full bulk gap and topological edge as well as higher-order corner states and (ii) with symmetry-protected bulk nodal points. Our results show the immense versatility of Shiba lattices to design the topology and sample geometry of 2D superconductors.

Rooted in its very thermodynamic identity, a superconductor can be destroyed through a sufficiently large magnetic field [1]. A local version of this effect can be observed at magnetic impurities in conventional s-wave superconductors: Yu-Shiba-Rusinov (YSR) states [2–4] – or Shiba states for short – are electronic modes localized at the impurity whose bound state energies lie within the superconducting gap. Through their spatial or energetic separation from all other excitations, they are well-controlled building blocks that allow one to create structures of bound states through magnetic impurity lattices on superconducting surfaces. This way, instead of destroying superconductivity, magnetic impurities can be used to design new superconducting electronic structures within the gap of a conventional s-wave superconductor with sought-after unconventional properties [5–7]. Previous experimental studies have in particular focused on one-dimensional (1D) chains [8–14], which, as envisioned in Kitaev's model [15], may host Majorana bound states at their ends. Two-dimensional (2D) Shiba lattices have been studied as potential realizations of chiral superconductivity with unidirectionally propagating Majorana edge modes [16]. Systems explored so far include lead monolayers covering magnetic cobalt islands [17], iron islands of monoatomic height on an oxygen reconstructed Re(0001) surface [18] and, more recently, van der Waals heterostructures consisting of monolayer $CrBr_3$ islands proximitized to superconducting $NbSe_2$[19].

Kitaev's Majorana chain and chiral superconductors are the elementary topological phases of spin-orbit coupled magnetic superconductors in 1D and 2D, respectively, according to the topological classification of electronic matter (class D in the tenfold way [20, 21]). However, if one includes topological phases protected through spatial symmetries, one uncovers the much richer variety of crystalline and boundary-obstructed topological superconductors [22–25]. In 2D, they can support two types of topologically protected boundary features: Majorana edge states and higher-order corner states [26–29]. They are, for instance, protected by mirror symmetries that leave the edge or corner invariant. Beyond fully gapped superconductors, crystalline symmetries can also protect gap nodes. The resulting nodal topological superconductors may support flatband Majorana edge states [30].

The objective of this study is to demonstrate the potential of Shiba lattices to create 2D crystalline topological superconductors. Specifically, we study Shiba lattices of chromium (Cr) atoms on the surface of superconducting niobium (Nb). Recent works about $3d$ transition metals on Nb already established the high versatility of this material platform [11, 31–33]. Using a scanning tunneling microscope, we (i) arrange the Cr into a desired finite-size lattice, (ii) characterize its topography, (iii) infer the magnetic structure from measurements with a spin-polarized tip, and (iv) spectroscopically characterize the electronic structure of the Shiba lattice with a superconducting tip. Here, we consider two distinct lattice arrangements – rectangular and rhombic – of the 2D Cr adatoms and build a total five different structures from them. We present theoretical and experimental evidence that points towards antiferromagnetic ordering of the magnetic moments in both lattices. In four of these structures, we observe enhanced density of states near zero bias at edges or corners — the charac-

teristics of topological crystalline superconductors. Only one structure is void of boundary modes. Through symmetry analysis and theoretical model building, we show how the edge modes can be naturally explained as topological flat bands protected by mirror symmetry. A more differentiated picture arises for the corner modes: On the rhombic lattice, they can be modeled as arising from a nodal Shiba lattice superconductor and are thus void of topological protection. On the rectangular lattice, theoretical modeling indicates a protection through higher-order topology. Our combined experimental and theoretical work highlights the enormous potential of Shiba lattices for creating crystalline topological superconductors as much as the need for scrutiny in interpreting spectroscopic data on them in favor of topological modes.

Design of Shiba lattices. To create Shiba lattices, we start by depositing Cr single atoms onto the surface of a Nb(110) single crystal prepared according to the procedure described in Ref. [34]. Niobium represents an optimal substrate offering the following advantages: (i) it has the largest superconducting energy gap ($2\Delta = 3.05$ meV) among all elemental superconductors, which facilitates the spectroscopic detection of in-gap states, and (ii) its high cohesive energy makes it possible to use atomic manipulation techniques to create nanostructures atom-by-atom using a bottom up approach [31, 32, 35, 36]. This is demonstrated in Figure 1a–b. Figure 1a shows a topographic image of single Cr adatoms randomly distributed onto the clean Nb(110) substrate, with the inset reporting an atomically resolved image of the Nb(110) surface. Figure 1b displays the very same sample region (red circles spotlight defects used as markers) after atomic manipulation [37] has been used to create distinct Cr nanostructures (highlighted by green circles).

Before analyzing 2D lattices, we examine the interaction between magnetic perturbations coupled to a superconducting condensate starting from the simplest case: an isolated magnetic impurity. Figure 1c reports scanning tunneling spectroscopy (STS) data acquired by positioning the tip on top of an isolated Cr adatom (green line) and on the bare Nb(110) surface (black line). To enhance the energy resolution and investigate the particle-hole asymmetry of low energy modes, measurements have been acquired using a bulk Nb tip, resulting in the typical convoluted spectrum of tip and sample superconducting energy gap [38] with the gray area corresponding to the tip superconducting gap $\pm\Delta_{\mathrm{tip}}$. Several peaks are visible within the superconducting gap for the Cr adatom. These peaks are direct signatures of the magnetic impurity–superconductor interaction, with magnetic moments locally breaking Cooper pairs and inducing the Shiba states [2–4, 39]. Their distinct orbital character can be visualized by spatially mapping their wave function distribution at specific sample biases (see colored diamonds and corresponding top panels in Figure 1c) [40, 41]. The strongest intensity is observed for the d_{z^2} orbital, which corresponds to the lowest-energy Shiba state located very close to $\pm\Delta_{\mathrm{tip}}$. Additional d_{xy} and d_{yz}-derived Shiba states are visible at higher energies [36, 42]. The existence of long range and highly anisotropic indirect interactions between Cr adatoms makes this platform amenable to create a large variety of distinct 2D Shiba lattices [36].

Figures 1d,e show the artificial 2D lattice structures subject to the present study. For each structure, an illustration of the position of the Cr adatoms (red dots) with respect to the underlying substrate (gray dots) is partially overlapped to the topographic images. Figure 1d (system A) corresponds to a rectangular lattice where adatoms are placed at a next-nearest neighbor distance with respect to the underlying Nb(110) lattice. This corresponds to a periodicity of 0.66 nm along the [001] direction (black line) and 0.93 nm along the $[1\bar{1}0]$ direction (green line). In Figure 1e (system B), Cr adatoms are arranged to create a rhombic lattice with adatoms placed at a distance of 0.85 nm along the $[1\bar{1}1]$ direction (cyan line). As discussed in the following, the different unit cells characterizing systems A and B as well as the choice of different terminations have far reaching implications on the emergence of distinct boundary modes.

To determine the magnetic coupling between the adatoms, Figures 1f–i report spin-resolved differential conductance maps ($\mathrm{d}I/\mathrm{d}U$) and the corresponding line profiles acquired using a Cr tip for chains oriented along three distinct crystallographic directions, i.e., [001] (Figure 1g), $[1\bar{1}0]$ (Figure 1h), and $[1\bar{1}1]$ (Figure 1i). For all directions, adatoms are placed at a distance equal to the periodicity along the corresponding crystallographic directions in the 2D lattices (see colored lines in Figure 1d-e). In order to stabilize the magnetic order against fluctuations, an external field of 0.7 T has been applied. All 1D chains are characterized by an alternating contrast, which is indicative of antiferromagnetic coupling between neighboring Cr adatoms. These measurements allow to infer the existence of an antiferromagnetic ground state for the two types of 2D lattices presented in Figure 1d-e.

Spectroscopy of Shiba lattices. When Cr impurities are brought close to each other, their Shiba states start overlapping and hybridizing [43–48]. For Cr adatoms arranged in 2D lattices, this leads to the formation of Shiba bands [31, 33, 49]. To scrutinize their emergence, full spectroscopic grids have been acquired for all lattices presented in the topographic images of Figures 2a–e. Contrary to real materials, where crystal terminations are generally dictated by either the growth mechanism or the cleavage plane, artificial 2D lattices built atom-by-atom allow to precisely engineer their boundaries. This makes possible to investigate the role of specifically designed lattice terminations.

The structures presented in Figures 2a–c, labeled by $\mathsf{A}_1, \mathsf{A}_2, \mathsf{A}_3$, are characterized by the same underlying lattice ordering of the Cr adatoms, corresponding to the rectangular lattice A. The distinction between the three structures lies in the choice of different terminations: system A_1 is terminated along the [001] and $[1\bar{1}0]$ directions, system A_2 is terminated along the $[1\bar{1}1]$ direction, and A_3

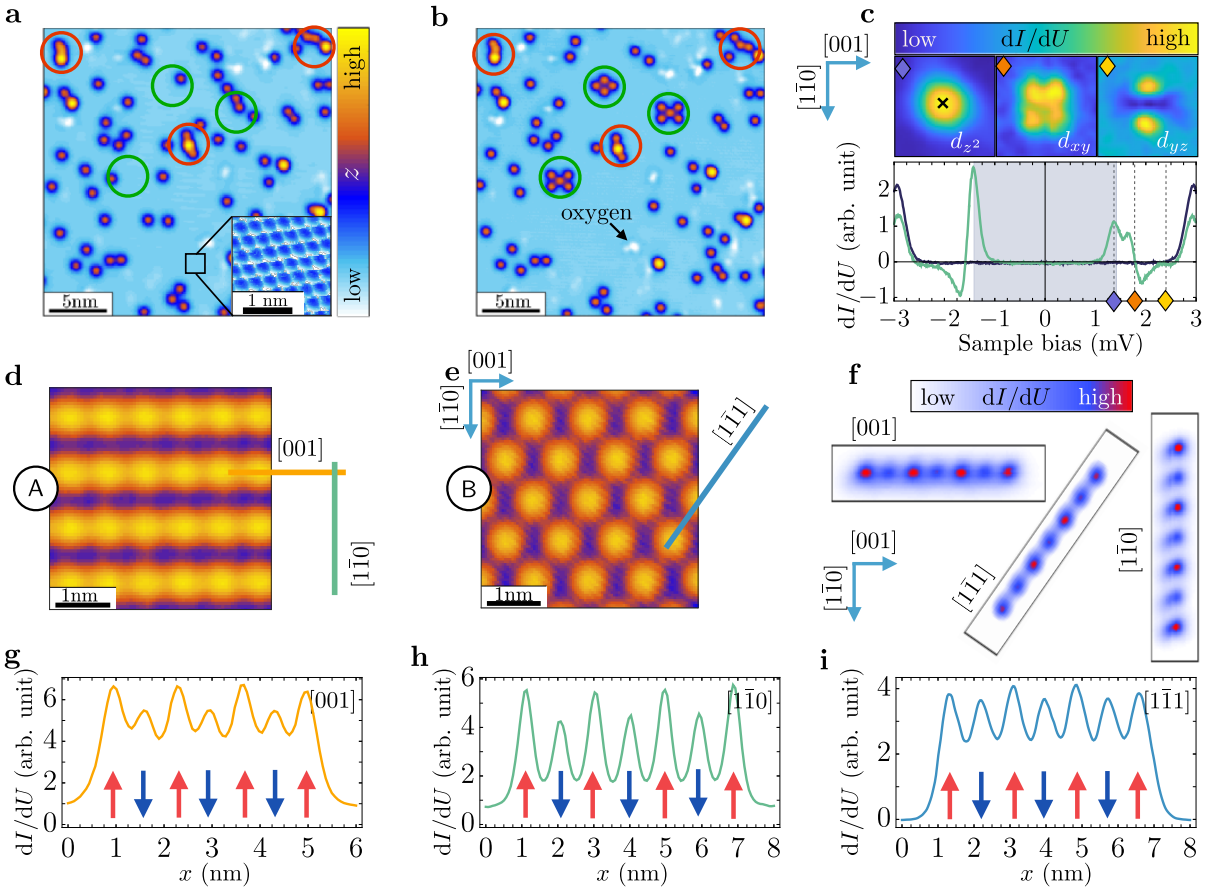

FIG. 1. **System characterization a** Topographic image of the Nb(110) surface after the deposition of Cr adatoms. The inset reports an atomically resolved image of the substrate. **b** Distinct unit cells assembled by positioning single Cr adatoms using atomic manipulation techniques, with the inset showing a single Cr adatom. **c** Spectroscopy acquired on an isolated Cr impurity (green line) showing multiple Shiba bound states. A spectrum acquired by positioning the tip over the substrate is given as reference (black line). Stabilization parameters: current 500 pA, sample bias −5 mV, modulation 50 µV. The dI/dU maps on the top display the spatial distribution of different Shiba bound states. The dominant Shiba state is of d_{z^2} character. **d-e** Topographic images of two types of Cr adatoms lattices scrutinized in this work. In system A Cr adatoms form a rectangular lattice, while in system B they form a rhombic lattice. For each structure, an illustration of the position of the Cr adatoms (red dots) with respect to the underlying substrate (blue dots) is overlapped to the topographic images. **g**–**i** dI/dU line profiles acquired on 1D chains using a spin-polarized tip. **f** dI/dU maps for each one of the chains in **g**–**i** taken in constant height mode. The alternating contrast is indicative of antiferromagnetic coupling between neighboring Cr adatoms. Scanning parameters: sample bias 0.27 mV, modulation 80 µV ([1$\bar{1}$0] and [001]) and sample bias 20 mV, modulation 1 mV ([1$\bar{1}$1]).

has a double-step as an edge along [2$\bar{2}$1]. For the systems in Figures 2d,e, the lattice corresponds to structure B, and is terminated along the [1$\bar{1}$1] direction in system B_1, while system B_2 is terminated along two distinct and orthogonal crystallographic directions, i.e. [001] and [1$\bar{1}$0].

The spectroscopic data reported in Figures 2a–e compare, for systems A_1, A_2, A_3, B_1, and B_2, dI/dU curves obtained by positioning the tip at distinct locations, namely: corners, edges, and bulk. Respective atomic positions are specified with corresponding colors in insets schematically depicting the lattices. The spectra in each structure are found to be position-dependent. In particular, the dI/dU spectra acquired at edges and corners show stronger spectral intensity at low energies with respect to the bulk. It is noteworthy that the spectral weight appears generally particle-hole asymmetric. Moreover, thermally excited states appear at energy $\Delta_{\mathrm{tip}} - \varepsilon_{\mathrm{YSR}}$ (see green diamond in Figure 2a) with $\varepsilon_{\mathrm{YSR}}$ corresponding to the energy of the Shiba states. These states are thermal replicas of states located at $-(\Delta_{\mathrm{tip}} + \varepsilon_{\mathrm{YSR}})$ and they appear inside the gray area corresponding to the tip superconducting gap [41]. To visualize the spatial distribution of the local density of states (LDOS), dI/dU maps at specific energies are reported as insets in Figures 2a–e identified by diamond markers. A comparison of these spectroscopic data makes it possible to scrutinize the response of the electronic properties to specifically designed lattice terminations.

Structures A_1, A_2, and A_3 are all built based on the rectangular lattice A. On the one hand, their bulk prop-

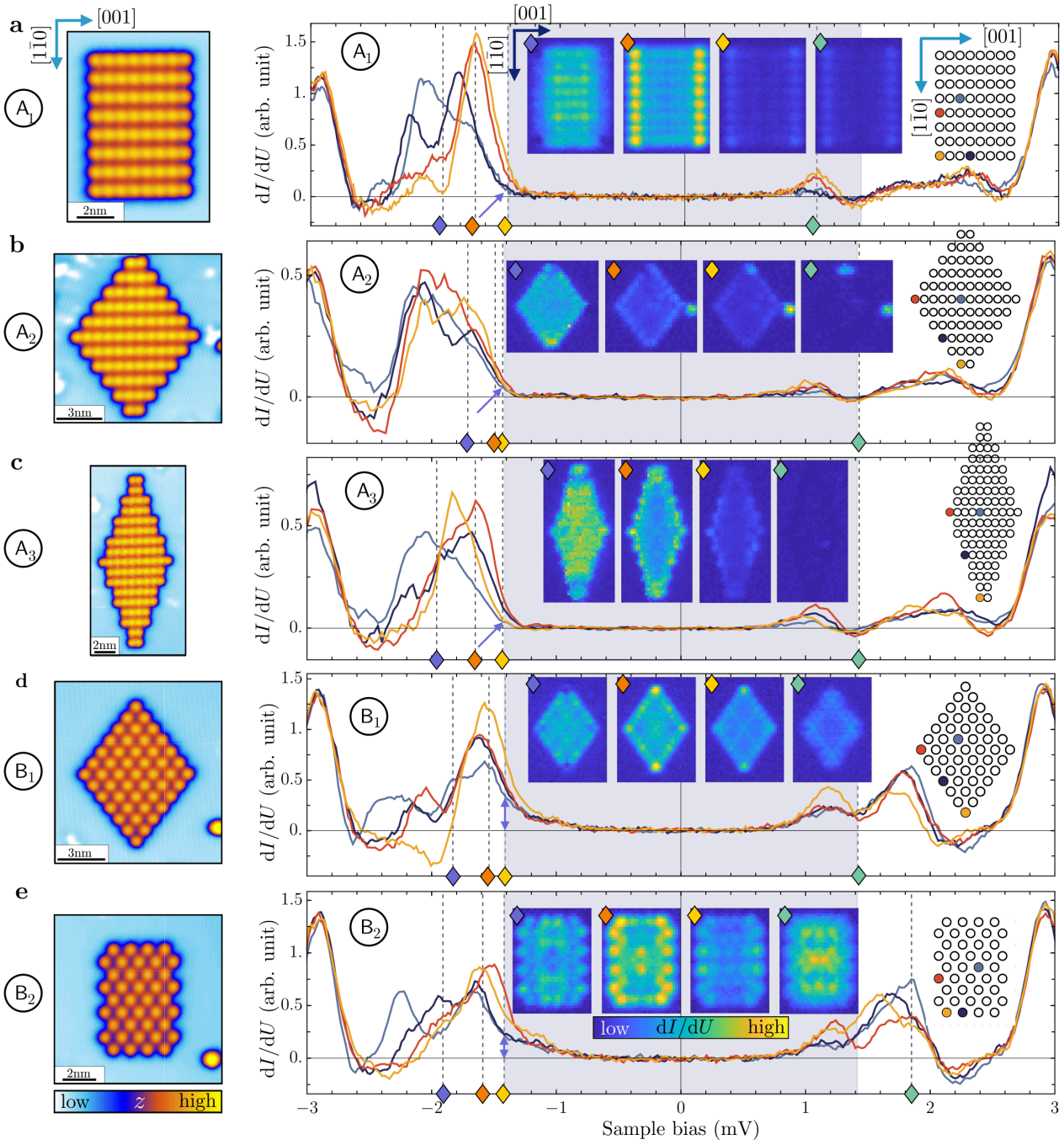

FIG. 2. **Spectroscopy of Shiba lattice superconductors** Topography of the Shiba 2D lattice termination (left) and differential conductance dI/dU measurements (right) acquired with a superconducting tip for four representative lattices sites (see color-coded sites on the insets showing the lattice structure scheme) at the two edges, a corner, and in the bulk of each structure for **a** system A_1, **b** system A_2, **c** system A_3 **d** system B_1, and **e** system B_2. Insets show dI/dU maps of the entire structure for selected energies marked in the main plots. The color-scale within the plots of each inset is identical, i.e., all maps referring to a specific termination have the same normalization. The gray area corresponds to the tip superconducting gap $\pm\Delta_{\rm tip}$. Stabilization parameters: current 500 pA, sample bias −5 mV, modulation 50 μV.

erties appear to be termination-independent. This is highlighted in two distinct ways: (i) the dI/dU curves acquired in the bulk (cyan line) are characterized by a similar lineshape with vanishing signal at zero energy ($\pm\Delta_{\rm tip}$ in our case because of the use of a superconducting tip); (ii) the spatially resolved dI/dU maps always show vanishing intensity inside the bulk at zero energy (yellow diamond) while the intensity becomes progressively stronger by increasing the bias (blue diamond). These observations are indicative of a Shiba lattice char-

acterized by a bulk gap, although a precise determination of the gap size is beyond the limits of our experimental energy resolution. On the other hand, the boundary modes are termination-dependent. A low energy edge mode is clearly detected in the rectangular system A_1, as demonstrated by the dI/dU map marked with an orange diamond in Figure 2a. The mode is localized at the boundary oriented along the $[1\bar{1}0]$ direction, while it is absent at the boundary oriented along the [001] direction. For terminations A_2 and A_3, a boundary mode is visible around the entire edge (see insets marked by an orange diamond). Moreover, system A_3 is characterized by a slightly enhanced low energy LDOS at the corners (red curve) with respect to the edge (blue curve). These results signal how the boundary electronic properties are qualitatively distinct in structures A_1, A_2, and A_3.

In sharp contrast to the rectangular case, the rhombic systems B_1 and B_2 appear gapless. This is demonstrated by the spectral intensity at the tip superconducting gap $\pm\Delta_{\text{tip}}$, which is far from being zero for dI/dU curves acquired in the bulk (see blue lines and arrows in Figures 2d–e). A gapless bulk is further confirmed by the dI/dU maps taken at $-\Delta_{\text{tip}}$ (see insets marked with a yellow diamond in Figures 2d–e). Although a stronger spectral intensity is observed at the boundaries, a finite LDOS is detected also in the bulk. Similar to the termination dependence observed in lattice A, systems B_1 and B_2 are also found to host distinct boundary modes: low energy corner modes are experimentally detected in system B_1 (see dI/dU map marked by an orange diamond in Figure 2d), while they are absent in system B_2.

Overall, these observations demonstrate that, starting from the very same building block (Cr adatoms in our case), it is possible to create both gapped (systems A_1, A_2, A_3) or gapless (system B_1 and B_2) Shiba lattices. This goal can be achieved by assembling 2D nanostructures characterized by distinct symmetries. Moreover, our results reveal that, even when considering the very same 2D structure, different lattice terminations play a crucial role in the emergence of distinct boundary modes.

Magnetic structure. To assess the magnetic states of the nanostructures, we complement the spin-resolved spectroscopic measurements with first-principles simulations. Specifically, we simulate systems A and B (Figures 1d,f) assuming periodic boundary conditions and extract the tensor of magnetic exchange interactions, more details are given in Methods. The Heisenberg exchange interaction J shown in Figure 3 is of antiferromagnetic nature at short adatom separation, and switches to ferromagnetic coupling depending on the distance between the Cr atoms. An oscillatory damped behavior is clearly observed. The Fermi surface of Nb is rather complex and anisotropic [36]. Therefore, the wavelength of the oscillations is not unique and depends on the direction along which the adatoms are positioned (see inset of Figure 3). Based on the calculated magnetic interactions, we find the structures designed experimentally to be antiferromagnetic, in agreement with the spin-polarized scanning tunneling microscopy (STM) measurements performed on the chains presented in Figures 1e,g,h. The Dzyaloshinskii-Moriya interaction is rather weak, which imposes a negligible tilting of the moments for the investigated finite structures.

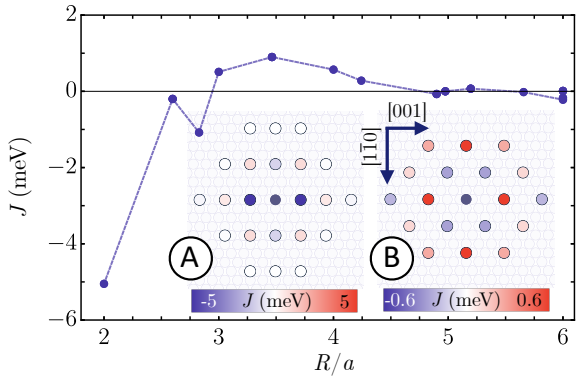

FIG. 3. **Magnetic exchange interactions.** Ab-initio Heisenberg exchange interactions J as function of distance R between Cr adatoms deposited on Nb(110), a being the bulk Nb lattice parameter [50]. Positive (negative) values correspond to ferromagnetic (antiferromagnetic) coupling. The lower inset illustrates the simulated lattices, where each circle is colored as function of the size of J with respect to the central atom (grey color).

Theoretical Analysis. To elucidate a potential topological origin of the observed edge and corner modes, we introduce minimal models for the Shiba lattices. Based on detailed symmetry considerations, we can draw conclusions about their topological properties that are robust independently of the specific choice of model parameters. We focus our models on the most pronounced and lowest energy Shiba orbital of a single Cr adatom, which is of d_{z^2} type (Figure 1c).

We developed two single-orbital tight-binding models to describe lattices composed of Shiba in-gap states. The models include up to next-to-nearest-neighbor hopping, Rashba spin-orbit coupling, the Hund's coupling between these electrons and the magnetic moment of Cr adatoms, and s-wave superconductivity induced from the bulk (see Methods and Supplementary Information). The two models are constrained by the symmetries of the rectangular and rhombic adatom lattices, respectively. In both cases, we assume antiferromagnetic ordering of the Cr moments as suggested by experimental measurements on adatom chains, shown in the lattice schemes of Figures 4a,e,i, and we consider spins pointing along the out of plane ([100]) direction. In Sec. I E of the Supplementary Information, we comment on the consequences of relaxing the latter assumption.

Focusing first on the rectangular lattice, the relevant spatio-temporal symmetries, which we denote by $\widetilde{M}_{x/y}$, are a composition of either of the mirror operations $M_{x/y}$ with the spinful time-reversal transformation $\mathcal{T}$, and $\widetilde{M}^2_{x/y} = (M_{x/y}\mathcal{T})^2 = +\mathbb{1}$, see Figure 4a (note that

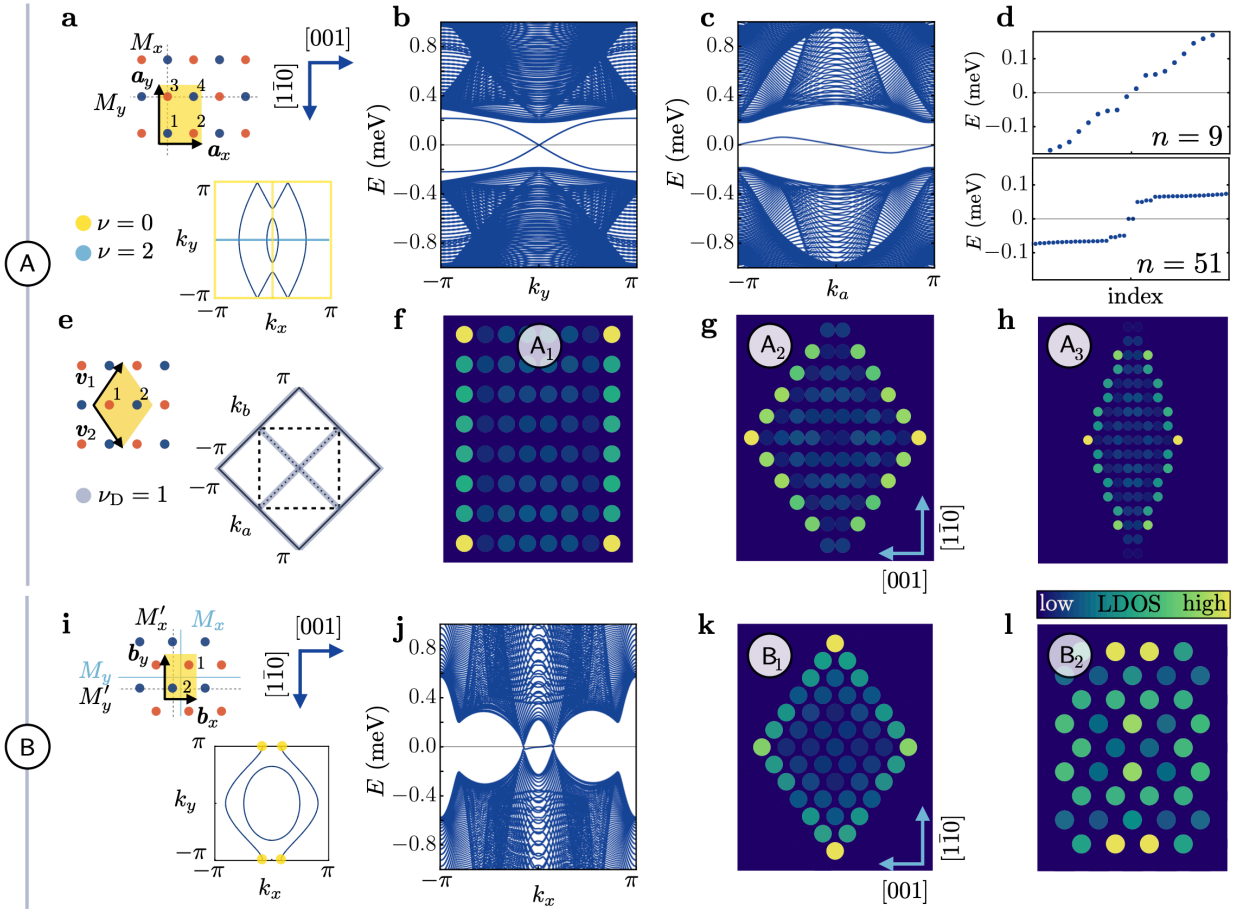

FIG. 4. **Theoretical modeling of Shiba lattice superconductors a** Upper panel: Lattice structure of system A, with the assumed antiferromagnetic ordering (blue: spin up, red: spin down). The unit cell is marked in yellow together with the intersection of mirror planes M_x and M_y with the plane of the Shiba lattice. Lower panel: Brillouin zone of the model for system A with normal state Fermi surfaces. Light-blue and yellow lines mark the mirror invariant paths along which the winding number topological invariant is defined. The two colors distinguish between zero (yellow) and non-zero (light-blue) topological invariants. **e** Choice of unit cell for the termination A_2 (upper panel) and the resulting unfolded Brillouin zone. Grey lines indicate particle-hole invariant lines, and the color marks the value of the Wilson loop invariant ν. **b**,**c** Ribbon spectra of the model for system A with open boundary conditions along the direction defined by the lattice vectors $\boldsymbol{a}_x$ and $\boldsymbol{v}_1$, respectively. The symmetry-protected topological boundary modes are visible in **b**. **d** Open boundary conditions spectra for the termination A_3 ($n = 9$, upper panel) and for an analogous termination with a larger size ($n = 51$, lower panel). Two zero energy modes are visible in both spectra, separated by a gap from the remaining energy modes. These correspond to the symmetry-protected higher-order topological corner modes discussed in the main text. **f**–**h** Local density of states (electronic part only) at zero energy of the model in the geometry of system **f** A_1, **g** A_2 and **h** A_3. A thermal broadening of 0.16 meV was used. **i** Upper panel: Lattice structure of systems B, with the assumed antiferromagnetic ordering (blue: spin up, red: spin down). The unit cell is marked in yellow together with the intersection of glide mirror planes M_x and M_y and mirror planes M'_x and M'_y with the plane of the Shiba lattice. The system is invariant under the composition of either of these mirror operations and time-reversal. Lower panel: Brillouin zone of the model for systems B with normal state Fermi surfaces. Yellow dots mark the position of symmetry-protected gap nodes in the presence of superconducting pairing. **j** Ribbon spectrum of the model for system $B_{1/2}$ with open boundary conditions in y direction. The bulk gap-closing points as well as a topological boundary mode is visible. **k** and **l** same as **f**–**h**, but for the system geometries B_1 and B_2, respectively.

$M_{x/y}$ and $\mathcal{T}$ individually are not symmetries of the system, as they flip all spins). The paths highlighted with colors in the Brillouin Zone of Figure 4a are left invariant under the action of particle-hole symmetry as well as $\widetilde{M}_{x/y}$. Thus, along these 1D subspaces of momentum space, the Hamiltonian belongs to the BDI class of the tenfold way topological classification of topological insulators and superconductors [21], with a $\mathbb{Z}$ topological classification. The corresponding topological invariant is the chiral winding number ν. Associated with the four $\widetilde{M}_{x/y}$-invariant lines are thus four 1D winding numbers: ν_{y,k_x}, for $k_x = 0, \pi$ and ν_{x,k_y}, for $k_y = 0, \pi$. For a range of the model parameters this invariant is non-trivial ($\nu = 2$) when computed along one of the lines, while the bulk is

gapped. The value $\nu_{x,k_y=0,\pi} = 2$ implies a geometry-dependent bulk-boundary correspondence: On the one hand, a ribbon of the system with open boundary conditions (OBC) in y direction will have a Dirac crossing of edge modes at zero energy and momentum $k_x = 0, \pi$ along the edge (and similar for $x \leftrightarrow y$), see Figure 4b. Specifically, for $\nu_{x,0} = 2$ and $\nu_{x,\pi} = \nu_{y,0} = \nu_{y,\pi} = 0$, these low energy modes are visible in the LDOS of a finite system, as boundary modes on the edges parallel y, as shown in Figure 4f. On the other hand, a geometry with an $\widetilde{M}_y$-invariant corner will support an isolated higher-order corner mode [26–29], as the one appearing in the LDOS of the termination in Figure 4h (see Sec. I B of the Supplementary Information). Two isolated zero energy modes are also visible in the open boundary condition spectra of this termination, see Figure 4d. These predictions are consistent with the experimental observations of an increased LDOS at the [001] edge of system A_1, as shown in the inset of Figure 2a, and at the corners of system A_3, see Figure 2c. Since the edge and corner modes are protected by crystalline lattice symmetries, the experimental terminations A_1 and A_3 realize a gapped topological crystalline superconductor.

A re-definition of the unit cell, according to Figure 4e, naturally leads to the modeling of the termination A_2. Once again, high symmetry lines in the Brillouin zone, corresponding to $k_a, k_b = 0, \pi$, are characterized by particle-hole symmetry. Hence, these 1D paths in momentum space belong to the D class of the tenfold way, with a $\mathbb{Z}_2$ classification. By a Wilson loop calculation [21], we find a non-trivial topological invariant $\nu = 1$ along each of these lines. This results in topological edge states (see Supplementary Material), visible in the ribbon spectra with open boundary conditions along k_b, characterised by zero energy modes at $k_a = 0, \pi$ (see Figure 4b), and an enhanced LDOS at the edges of an open boundary structure (see Figure 4g). In contrast to the edge and corner modes of Figure 4f,h, the edge modes in Figure 4g do not require crystalline symmetries to be topologically protected. Once more, this prediction is in agreement with the experimental observations of an enhanced LDOS at the edges of system A_2 (see Figure 2b).

For the rhombic lattice, the relevant symmetries are the glide mirror symmetries $M_{x/y}$ and the composition of the two mirror operations $M'_{x/y}$ with time reversal, again denoted as $\widetilde{M}_{x/y} = M'_{x/y}\mathcal{T}$, where $\widetilde{M}^2_{x/y} = +\mathbb{1}$ (see Figure 4i). For this case, we find an energy structure with gapless nodal points whose degeneracy is protected by glide mirrors $M_{x/y}$ combined with particle-hole symmetry (see Supplementary Information): any crossing of the normal-state Fermi surface with the Brillouin zone boundary becomes a symmetry-protected nodal point of the gap once superconductivity is included (yellow dots in Figure 4i). Furthermore, along the paths $\boldsymbol{k} = (k_x, k_y = 0)$ and $\boldsymbol{k} = (k_x = 0, k_y)$ in the Brillouin zone, along which there is generically a full superconducting gap, the Hamiltonian belongs to the BDI class by virtue of $\widetilde{M}_{x/y}$ symmetry. As in the case of the rectangular lattice, a non-trivial chiral winding number along one of these paths results in a zero-energy mode in a ribbon geometry. For a specific choice of model parameters, this is shown in the ribbon spectrum (Figure 4j). However, in contrast to the case of the rectangular lattice, these edge states coexist with the bulk gapless modes. Nevertheless, they result in an enhanced LDOS at the corners of the lattice geometry B_1 (Figure 4k), which agrees with the experimental observations (Figure 2d). As the bulk is gapless, this mode is not topologically protected. For the lattice geometry B_2, our model has a rather featureless LDOS at zero energy with slightly enhanced spectral weight at the edges (Figure 4l), consistent with the experimental measurements (Figure 2e). The latter example shows that the interpretation of LDOS in Shiba lattices can easily be misguided, as the corners in Figure 4k could be misinterpreted as carrying Majorana zero modes. Nevertheless, our theoretical models for the rectangular and rhombic Shiba lattices are in topological crystalline superconducting phases with gapped and gapless 2D bulk, respectively. They demonstrate how abundant topological phases are in spin-orbit coupled Shiba lattices.

Discussion. Our work explores a novel route towards constructing 2D topological (crystalline) superconductors, namely a bottom-up approach where a lattice system is built up atom-by-atom.

This bears the potential to realize a large variety of artificial 2D Shiba lattices in a clean and disorder-free platform and specifically enables the investigation of topological crystalline superconducting phases which remained largely unexplored so far. The combined possibilities of designing lattices characterized by different symmetries and the use of distinct magnetic elements as building blocks offer an unprecedented flexibility to artificially create and control topologically protected superconducting states.

We have constructed two lattices which we theoretically expect to realize a fully gapped and a nodal topological crystalline superconductor, respectively. Our data are remarkably consistent with the theoretical predictions of edge and higher-order corner modes. At the same time, we caution that these modes are likely not isolated Majorana states, as we have only focused on the experimentally most prominent Shiba bound state of the adatoms. The other Shiba bound states may contribute additional modes not detectable within our experimental resolution. To further solidify our findings, it is desirable to reach lower temperatures to disentangle the intrinsic bandwidth of the boundary modes from thermal broadening effects and assemble larger systems. Another aspect motivating further investigations is the stark particle-hole asymmetry observed in our data.

More broadly, future directions to be explored with this platform can rely on a wealth of theoretical predictions and include realizing other lattice geometries and terminations, as well as intentionally crafted lattice dis-

locations and domain walls. Specifically, the realization of lattices hosting bulk flat bands, such as the Kagome and Lieb lattices, may pave the way to the study of interaction effects in Shiba bands.

[1] W. Meissner and R. Ochsenfeld. Ein neuer effekt bei eintritt der supraleitfähigkeit. *Naturwissenschaften*, 21(44):787–788, 1933.

[2] Luh Yu. Bound state in superconductors with paramagnetic impurities. *Acta Phys. Sin.*, 21:75–91, 1965.

[3] Hiroyuki Shiba. Classical Spins in Superconductors. *Progress of Theoretical Physics*, 40(3):435–451, 1968.

[4] A. I. Rusinov. Superconcductivity near a paramagnetic impurity. *Zh. Eksp. Teor. Fiz. Pisma Red.*, 9, 1968. [JETP Lett. 9, 85 (1969)].

[5] S. Nadj-Perge, I. K. Drozdov, B. A. Bernevig, and Ali Yazdani. Proposal for realizing Majorana fermions in chains of magnetic atoms on a superconductor. *Phys. Rev. B*, 88:020407, Jul 2013.

[6] Falko Pientka, Yang Peng, Leonid Glazman, and Felix von Oppen. Topological superconducting phase and Majorana bound states in Shiba chains. *Physica Scripta*, T164:014008, aug 2015.

[7] P. M. R. Brydon, S. Das Sarma, Hoi-Yin Hui, and Jay D. Sau. Topological Yu-Shiba-Rusinov chain from spin-orbit coupling. *Phys. Rev. B*, 91:064505, Feb 2015.

[8] Stevan Nadj-Perge, Ilya K. Drozdov, Jian Li, Hua Chen, Sangjun Jeon, Jungpil Seo, Allan H. MacDonald, B. Andrei Bernevig, and Ali Yazdani. Observation of Majorana fermions in ferromagnetic atomic chains on a superconductor. *Science*, 346(6209):602–607, 2014.

[9] Michael Ruby, Falko Pientka, Yang Peng, Felix von Oppen, Benjamin W. Heinrich, and Katharina J. Franke. End states and subgap structure in proximity-coupled chains of magnetic adatoms. *Phys. Rev. Lett.*, 115:197204, Nov 2015.

[10] Michael Ruby, Benjamin W. Heinrich, Yang Peng, Felix von Oppen, and Katharina J. Franke. Exploring a proximity-coupled Co chain on Pb(110) as a possible Majorana platform. *Nano Letters*, 17(7):4473–4477, 07 2017.

[11] Lucas Schneider, Sascha Brinker, Manuel Steinbrecher, Jan Hermenau, Thore Posske, Manuel dos Santos Dias, Samir Lounis, Roland Wiesendanger, and Jens Wiebe. Controlling in-gap end states by linking nonmagnetic atoms and artificially-constructed spin chains on superconductors. *Nature Communications*, 11(1):4707, 2020.

[12] Cristina Mier, Jiyoon Hwang, Jinkyung Kim, Yujeong Bae, Fuyuki Nabeshima, Yoshinori Imai, Atsutaka Maeda, Nicolás Lorente, Andreas Heinrich, and Deung-Jang Choi. Atomic manipulation of in-gap states in the $\beta-\mathrm{bi_2Pd}$ superconductor. *Phys. Rev. B*, 104:045406, Jul 2021.

[13] Lucas Schneider, Philip Beck, Jannis Neuhaus-Steinmetz, Levente Rózsa, Thore Posske, Jens Wiebe, and Roland Wiesendanger. Precursors of Majorana modes and their length-dependent energy oscillations probed at both ends of atomic Shiba chains. *Nature Nanotechnology*, 2022.

[14] Howon Kim, Alexandra Palacio-Morales, Thore Posske, Levente Rózsa, Krisztián Palotás, László Szunyogh, Michael Thorwart, and Roland Wiesendanger. Toward tailoring majorana bound states in artificially constructed magnetic atom chains on elemental superconductors. *Science Advances*, 4(5):eaar5251, 2018.

[15] A Yu Kitaev. Unpaired Majorana fermions in quantum wires. *Physics-Uspekhi*, 44(10S):131–136, oct 2001.

[16] Jian Li, Titus Neupert, Zhijun Wang, A. H. MacDonald, A. Yazdani, and B. Andrei Bernevig. Two-dimensional chiral topological superconductivity in Shiba lattices. *Nature Communications*, 7(1), 2016.

[17] Gerbold C. Ménard, Sébastien Guissart, Christophe Brun, Raphaël T. Leriche, Mircea Trif, François Debontridder, Dominique Demaille, Dimitri Roditchev, Pascal Simon, and Tristan Cren. Two-dimensional topological superconductivity in pb/co/si(111). *Nature Communications*, 8(1):2040, 2017.

[18] Alexandra Palacio-Morales, Eric Mascot, Sagen Cocklin, Howon Kim, Stephan Rachel, Dirk K. Morr, and Roland Wiesendanger. Atomic-scale interface engineering of Majorana edge modes in a 2d magnet-superconductor hybrid system. *Science Advances*, 5(7):eaav6600, 2019.

[19] Shawulienu Kezilebieke, Md Nurul Huda, Viliam Vaňo, Markus Aapro, Somesh C. Ganguli, Orlando J. Silveira, Szczepan Głodzik, Adam S. Foster, Teemu Ojanen, and Peter Liljeroth. Topological superconductivity in a van der Waals heterostructure. *Nature*, 588(7838):424–428, 2020.

[20] Alexei Kitaev. Periodic table for topological insulators and superconductors. *AIP Conference Proceedings*, 1134(1):22–30, 2009.

[21] Shinsei Ryu, Andreas P. Schnyder, Akira Furusaki, and Andreas W. W. Ludwig. Topological insulators and superconductors: tenfold way and dimensional hierarchy. *New Journal of Physics*, 12:065010, 2010.

[22] Seishiro Ono, Hoi Chun Po, and Haruki Watanabe. Refined symmetry indicators for topological superconductors in all space groups. *Science Advances*, 6(18):eaaz8367, 2020.

[23] Ken Shiozaki and Masatoshi Sato. Topology of crystalline insulators and superconductors. *Phys. Rev. B*, 90:165114, Oct 2014.

[24] Qing-Ze Wang and Chao-Xing Liu. Topological nonsymmorphic crystalline superconductors. *Phys. Rev. B*, 93:020505, Jan 2016.

[25] Xianxin Wu, Wladimir A. Benalcazar, Yinxiang Li, Ronny Thomale, Chao-Xing Liu, and Jiangping Hu. Boundary-obstructed topological high-t_c superconductivity in iron pnictides. *Phys. Rev. X*, 10:041014, Oct 2020.

[26] Wladimir A. Benalcazar, B. Andrei Bernevig, and Taylor L. Hughes. Quantized electric multipole insulators. *Science*, 357(6346):61–66, 2017.

[27] Frank Schindler, Ashley M. Cook, G. Vergniory, Maia, Zhijun Wang, S. P. Parkin, Stuart, Andrei Bernevig, and Titus Neupert. Higher-order topological insulators. *Science Advances*, 4, 2018.

[28] Max Geier, Luka Trifunovic, Max Hoskam, and Piet W. Brouwer. Second-order topological insulators and su-

perconductors with an order-two crystalline symmetry. *Phys. Rev. B*, 97:205135, May 2018.

[29] Eslam Khalaf. Higher-order topological insulators and superconductors protected by inversion symmetry. *Phys. Rev. B*, 97:205136, May 2018.

[30] Andreas P Schnyder and Philip M R Brydon. Topological surface states in nodal superconductors. *Journal of Physics: Condensed Matter*, 27(24):243201, may 2015.

[31] Lucas Schneider, Philip Beck, Thore Posske, Daniel Crawford, Eric Mascot, Stephan Rachel, Roland Wiesendanger, and Jens Wiebe. Topological Shiba bands in artificial spin chains on superconductors. *Nature Physics*, 17(8):943–948, 2021.

[32] Felix Friedrich, Robin Boshuis, Matthias Bode, and Artem Odobesko. Coupling of Yu-Shiba-Rusinov states in one-dimensional chains of Fe atoms on Nb(110). *Phys. Rev. B*, 103:235437, Jun 2021.

[33] Felix Küster, Sascha Brinker, Richard Hess, Daniel Loss, Stuart Parkin, Jelena Klinovaja, Samir Lounis, and Paolo Sessi. Non-Majorana modes in diluted spin chains proximitized to a superconductor. 2021.

[34] Artem B. Odobesko, Soumyajyoti Haldar, Stefan Wilfert, Jakob Hagen, Johannes Jung, Niclas Schmidt, Paolo Sessi, Matthias Vogt, Stefan Heinze, and Matthias Bode. Preparation and electronic properties of clean superconducting Nb(110) surfaces. *Phys. Rev. B*, 99:115437, Mar 2019.

[35] Artem Odobesko, Domenico Di Sante, Alexander Kowalski, Stefan Wilfert, Felix Friedrich, Ronny Thomale, Giorgio Sangiovanni, and Matthias Bode. Observation of tunable single-atom yu-shiba-rusinov states. *Phys. Rev. B*, 102:174504, Nov 2020.

[36] Felix Küster, Sascha Brinker, Samir Lounis, Stuart S. P. Parkin, and Paolo Sessi. Long range and highly tunable interaction between local spins coupled to a superconducting condensate. *Nature Communications*, 12(1):6722, 2021.

[37] Joseph A. Stroscio and D. M. Eigler. Atomic and molecular manipulation with the scanning tunneling microscope. *Science*, 254(5036):1319–1326, 1991.

[38] K. J. Franke, G. Schulze, and J. I. Pascual. Competition of superconducting phenomena and Kondo screening at the nanoscale. *Science*, 332(6032):940–944, 2011.

[39] Ali Yazdani, B. A. Jones, C. P. Lutz, M. F. Crommie, and D. M. Eigler. Probing the local effects of magnetic impurities on superconductivity. *Science*, 275(5307):1767–1770, 1997.

[40] Michael Ruby, Yang Peng, Felix von Oppen, Benjamin W. Heinrich, and Katharina J. Franke. Orbital picture of Yu-Shiba-Rusinov multiplets. *Phys. Rev. Lett.*, 117:186801, Oct 2016.

[41] Deung-Jang Choi, Carmen Rubio-Verdú, Joeri de Bruijckere, Miguel M. Ugeda, Nicolás Lorente, and Jose Ignacio Pascual. Mapping the orbital structure of impurity bound states in a superconductor. *Nature Communications*, 8(1):15175, 2017.

[42] Felix Küster, Ana M. Montero, Filipe S. M. Guimarães, Sascha Brinker, Samir Lounis, Stuart S. P. Parkin, and Paolo Sessi. Correlating Josephson supercurrents and Shiba states in quantum spins unconventionally coupled to superconductors. *Nature Communications*, 12(1):1108, 2021.

[43] Michael Ruby, Benjamin W. Heinrich, Yang Peng, Felix von Oppen, and Katharina J. Franke. Wave-function hybridization in Yu-Shiba-Rusinov dimers. *Phys. Rev. Lett.*, 120:156803, Apr 2018.

[44] Philip Beck, Lucas Schneider, Levente Rózsa, Krisztián Palotás, András Lászlóffy, László Szunyogh, Jens Wiebe, and Roland Wiesendanger. Spin-orbit coupling induced splitting of Yu-Shiba-Rusinov states in antiferromagnetic dimers. *Nature Communications*, 12(1):2040, 2021.

[45] Hao Ding, Yuwen Hu, Mallika T. Randeria, Silas Hoffman, Oindrila Deb, Jelena Klinovaja, Daniel Loss, and Ali Yazdani. Tuning interactions between spins in a superconductor. *Proceedings of the National Academy of Sciences*, 118(14):e2024837118, 2021.

[46] Shawulienu Kezilebieke, Marc Dvorak, Teemu Ojanen, and Peter Liljeroth. Coupled Yu–Shiba–Rusinov states in molecular dimers on $NbSe_2$. *Nano Letters*, 18(4):2311–2315, 04 2018.

[47] Deung-Jang Choi, Carlos García Fernández, Edwin Herrera, Carmen Rubio-Verdú, Miguel M. Ugeda, Isabel Guillamón, Hermann Suderow, José Ignacio Pascual, and Nicolás Lorente. Influence of magnetic ordering between Cr adatoms on the Yu-Shiba-Rusinov states of the $\beta-bi_2Pd$ superconductor. *Phys. Rev. Lett.*, 120:167001, Apr 2018.

[48] Felix Küster, Ana M. Montero, Filipe S. M. Guimarães, Sascha Brinker, Samir Lounis, Stuart S. P. Parkin, and Paolo Sessi. Correlating Josephson supercurrents and Shiba states in quantum spins unconventionally coupled to superconductors. *Nature Communications*, 12(1):1108, February 2021.

[49] Eva Liebhaber, Lisa M. Rütten, Gaël Reecht, Jacob F. Steiner, Sebastian Rohlf, Kai Rossnagel, Felix von Oppen, and Katharina J. Franke. Quantum spins and hybridization in artificially-constructed chains of magnetic adatoms on a superconductor. *Nature Communications*, 13(1):2160, 2022.

[50] Multiple data points at the same r/a but with distinct values of j correspond to symmetry non-equivalent sites.

[51] N Papanikolaou, R Zeller, and P H Dederichs. Conceptual improvements of the KKR method. *Journal of Physics: Condensed Matter*, 14(11):2799, 2002.

[52] D. S. G. Bauer. Development of a relativistic full-potential first-principles multiple scattering Green function method applied to complex magnetic textures of nanostructures at surfaces. *Forschungszentrum Jülich*, 2014.

[53] S. H. Vosko, L. Wilk, and M. Nusair. Accurate spin-dependent electron liquid correlation energies for local spin density calculations: a critical analysis. *Canadian Journal of Physics*, 58(8):1200–1211, 1980.

[54] A. I. Liechtenstein, M. I. Katsnelson, V. P. Antropov, and V. A. Gubanov. Local spin density functional approach to the theory of exchange interactions in ferromagnetic metals and alloys. *Journal of Magnetism and Magnetic Materials*, 67(1):65–74, May 1987.

[55] H. Ebert and S. Mankovsky. Anisotropic exchange coupling in diluted magnetic semiconductors: Ab initio spin-density functional theory. *Physical Review B*, 79(4):045209, January 2009.

STM and STS measurements. All experiments were performed in a ultra-high vacuum STM setup, operated at a temperature of 1.9 K. The bulk single-crystal Nb(110) substrate was cleaned by repeatedly flashing the surface to about 2300 K. Cr adatoms were deposited in-situ and with the substrate below a temperature of 15 K. Cr adatoms could be moved with atomic precision by approaching them with the STM tip in constant current mode and a setpoint of −5 mV; 70 nA. dI/dU spectra were taken by lock-in technique.

Technical details/Method – Ab-initio. The ab-initio simulations are based on the the scalar-relativistic full-electron full-potential Korringa-Kohn-Rostoker (KKR) Green function augmented self-consistently with spin-orbit interaction [51, 52]. The local spin density approximation (LSDA) is employed for the evaluation of the exchange-correlation potential [53]. We assume an angular momentum cutoff at $\ell_{\max} = 3$ for the orbital expansion of the Green function. A slab is used to model the Nb surface by considering 22 layers enclosed by two vacuum regions with a thickness of 9.33 Å each. On top of one of the Nb surfaces we place the diluted Cr layer such that the adatoms reside on the hollow stacking site relaxed towards the surface by 20 % of the inter-layer distance of the underlying Nb(110) surface. This was shown to be the energetically favored stacking of single adatoms in Ref. 48. The magnetic exchange interactions were obtained using the magnetic force theorem in the frozen-potential approximation and the infinitesimal rotation method [54, 55].

Tight-Binding Models For the description of the lattice terminations A and B, we construct a minimal tight-binding model for d_{z^2}-like orbitals. For A, the normal state Hamiltonian of the lattice, with reference to the unit cell shown in Figure 4a, is

$$\begin{aligned}\hat{H}_{\rm n} = \sum_{\boldsymbol{r},\sigma}\Big\{ &\sum_{l=1}^{4}[J\sigma(-1)^{f(l)}-\mu]\hat{c}^{\dagger}_{\boldsymbol{r}\sigma l}\hat{c}_{\boldsymbol{r}\sigma l}\\ &+\sum_{n=0,1}\Big[\sum_{l=1,3}t_x(\hat{c}^{\dagger}_{\boldsymbol{r}\sigma l}\hat{c}_{\boldsymbol{r}+n\boldsymbol{a}_x\sigma l+1}+h.c.)\\ &+\sum_{l=1,2}t_y(\hat{c}^{\dagger}_{\boldsymbol{r}\sigma l}\hat{c}_{\boldsymbol{r}+n\boldsymbol{a}_y\sigma l+2}+h.c.)\\ &+\sum_{\sigma',l=1,3}\lambda_x \mathrm{i}\sigma^{y}_{\sigma\sigma'}(-1)^{n+\tilde{l}}(\hat{c}^{\dagger}_{\boldsymbol{r}\sigma l}\hat{c}_{\boldsymbol{r}+n\boldsymbol{a}_x\sigma' l+1}+h.c.)\\ &+\sum_{\sigma',l=1,2}\lambda_y \mathrm{i}\sigma^{x}_{\sigma\sigma'}(-1)^{n+l}(\hat{c}^{\dagger}_{\boldsymbol{r}\sigma l}\hat{c}_{\boldsymbol{r}+n\boldsymbol{a}_y\sigma' l+2}+h.c.)\Big]\Big\},\end{aligned} \tag{1}$$

with $f(l) : \{1,2,3,4\} \to \{0,1,1,0\}$ reproducing the antiferromagnetic pattern in the unit cell, and $\tilde{l} = 1,2$ for $l = 1,3$ respectively. Here, J indicates the Hund's coupling strength between electrons and Cr magnetic moments, μ the chemical potential, $t_{x/y}$ and $\lambda_{x/y}$ are hopping and spin-orbit-coupling (SOC) amplitudes, while σ^i's indicate Pauli matrices. The Bogoliubov de Gennes Hamiltonian of the Shiba lattice then becomes

$$\hat{H} = \sum_{\boldsymbol{k}} \Psi^{\dagger}_{\boldsymbol{k}} \begin{pmatrix} H_{\rm n}(\boldsymbol{k}) & \Delta \\ \Delta^{\dagger} & -H^{*}_{\rm n}(-\boldsymbol{k}) \end{pmatrix} \Psi_{\boldsymbol{k}} \tag{2}$$

with $H_{\rm n}(\boldsymbol{k})$ the Bloch Hamiltonian derived from (1), $\Delta = \mathbb{1}_{4\times4} \otimes (\mathrm{i}\sigma^y)$ the s-wave superconducting pairing and spinor $\Psi_{\boldsymbol{k}} = (\hat{c}_{\boldsymbol{k}\uparrow1}, \hat{c}_{\boldsymbol{k}\downarrow1}, ..., \hat{c}_{\boldsymbol{k}\uparrow4}, \hat{c}_{\boldsymbol{k}\downarrow4}, \hat{c}^{\dagger}_{-\boldsymbol{k}\uparrow1}, \hat{c}^{\dagger}_{-\boldsymbol{k}\downarrow1}, ..., \hat{c}^{\dagger}_{-\boldsymbol{k}\uparrow4}, \hat{c}^{\dagger}_{-\boldsymbol{k}\downarrow4})$. In the chiral symmetry ($\mathcal{C} = \mathcal{P}\widetilde{\mathcal{T}}$) basis, the Bloch Hamiltonian (2) takes the form

$$H(\boldsymbol{k}) = \begin{pmatrix} 0 & q(\boldsymbol{k}) \\ q^{\dagger}(\boldsymbol{k}) & 0 \end{pmatrix}, \tag{3}$$

where we introduced the chiral Hamiltonian $q(\boldsymbol{k})$. The chiral winding number $\nu \in \mathbb{Z}$ of the BDI class of the tenfold way can be obtained by computing the following integral along 1D closed paths in the Brillouin zone [21]

$$\nu = -\frac{\mathrm{i}}{2\pi}\int_{-\pi}^{\pi} dk\ \mathrm{Tr}[q^{\dagger}(k)\partial_k q(k)], \tag{4}$$

where we parametrized the path by the variable $k \in [-\pi,\pi)$. For example, for $\nu_{x,k_x=0}$, the relevant path in momentum space is defined by $\boldsymbol{k} = (0,k)$, with $k \in [-\pi,\pi)$. This chiral winding number is the BDI class topological invariant mentioned in the text and highlighted in Figure 4a.

For the lattice of type B, and with reference to the unit cell shown in Figure 4e, the normal state Hamiltonian is

$$\begin{aligned}\hat{H}_{\rm n} = \sum_{\boldsymbol{r},\sigma}\Big\{ &\sum_{l=1}^{2}[J\sigma(-1)^{l}-\mu]\hat{c}^{\dagger}_{\boldsymbol{r}\sigma l}\hat{c}_{\boldsymbol{r}\sigma l}\\ &+\sum_{\boldsymbol{b}}\Big[t(\hat{c}^{\dagger}_{\boldsymbol{r}\sigma 1}\hat{c}_{\boldsymbol{r}+\boldsymbol{b}\sigma 2}+h.c.)\\ &\quad+\sum_{\sigma'}\mathrm{i}(\boldsymbol{d}(\boldsymbol{b})\times\boldsymbol{\sigma})_{\sigma\sigma'}(\hat{c}^{\dagger}_{\boldsymbol{r}\sigma 1}\hat{c}_{\boldsymbol{r}+\boldsymbol{b}\sigma' 2}+h.c.)\Big]\\ &+\sum_{l=1}^{2}\Big[t_x(\hat{c}^{\dagger}_{\boldsymbol{r}\sigma l}\hat{c}_{\boldsymbol{r}+\boldsymbol{b}_x\sigma l}+h.c.)\\ &\quad+t_y(\hat{c}^{\dagger}_{\boldsymbol{r}\sigma l}\hat{c}_{\boldsymbol{r}+\boldsymbol{b}_y\sigma l}+h.c.)\\ &\quad+\sum_{\sigma'}\lambda_x(\mathrm{i}\sigma^{y}_{\sigma\sigma'}\hat{c}^{\dagger}_{\boldsymbol{r}\sigma l}\hat{c}_{\boldsymbol{r}+\boldsymbol{b}_x\sigma' l}+h.c.)\\ &\quad+\lambda_y(\mathrm{i}\sigma^{x}_{\sigma\sigma'}\hat{c}^{\dagger}_{\boldsymbol{r}\sigma l}\hat{c}_{\boldsymbol{r}+\boldsymbol{b}_y\sigma' l}+h.c.)\Big]\Big\},\end{aligned} \tag{5}$$

where the sum runs over $\boldsymbol{b} \in \{0, \boldsymbol{b}_x, \boldsymbol{b}_y, \boldsymbol{b}_x+\boldsymbol{b}_y\}$, t and $\boldsymbol{d}(\boldsymbol{b}) = d_x(\boldsymbol{b})\hat{\boldsymbol{x}} + d_y(\boldsymbol{b})\hat{\boldsymbol{y}}$ are nearest-neighbor hopping and spin orbit-coupling vector, $t_{x/y}$ and $\lambda_{x/y}$ are next-to-nearest-neighbor hoppings and Rashba SOC amplitude respectively. In the last line, we took into account next-to-nearest neighbor hoppings to lift the degeneracy of additional non-symmetry protected gapless points. The Bogoliubov de Gennes Hamiltonian assumes the same structure of the one in Eq. (2), with $H_{\rm n}(\boldsymbol{k})$ obtained from (5), $\Delta = \mathbb{1}_{2\times2} \otimes (\mathrm{i}\sigma^y)$ and spinor $\Psi_{\boldsymbol{k}} = (\hat{c}_{\boldsymbol{k}\uparrow1}, \hat{c}_{\boldsymbol{k}\downarrow1}, \hat{c}_{\boldsymbol{k}\uparrow2}, \hat{c}_{\boldsymbol{k}\downarrow2}, \hat{c}^{\dagger}_{-\boldsymbol{k},1,\uparrow}, \hat{c}^{\dagger}_{-\boldsymbol{k}\downarrow1}, \hat{c}^{\dagger}_{-\boldsymbol{k}\uparrow2}, \hat{c}^{\dagger}_{-\boldsymbol{k}\downarrow2})$.

I. ACKNOWLEDGEMENTS

AA and SL thank M. dos Santos Dias and S. Brinker for fruitful discussions. GW acknowledges NCCR MARVEL funding from the Swiss National Science Foundation. TN acknowledges funding from the European Research Council (ERC) under the European Union's Horizon 2020 research and innovation programm (ERC-StG-Neupert-757867-PARATOP). MOS acknowledges funding from the Swiss National Science Foundation (Project 200021E_198011) as part of the FOR 5249 (QUAST) lead by the Deutsche Forschungsgemeinschaft (DFG, German Research Foundation). AA is funded by the the Palestinian-German Science Bridge (BMBF grant number 01DH16027) and her DFT simulations were made on the supercomputer JURECA at Forschungszentrum Jülich with computing time granted through JARA. RT acknowledges the Wuerzburg-Dresden Cluster of Excellence ct.qmat.

— Supplementary Material —
Building crystalline topological superconductors from Shiba lattices

Martina O. Soldini[1], Felix Küster[2], Glenn Wagner[1], Souvik Das[2], Amal Aldarawsheh[3,5], Ronny Thomale[4,6], Samir Lounis[3,5], Stuart S. P. Parkin[2], Paolo Sessi[2], Titus Neupert[1].

[1] *University of Zurich, Winterthurerstrasse 190, 8057 Zurich, Switzerland,*
[2] *Max Planck Institute of Microstructure Physics, Halle, Germany,*
[3] *Peter Grünberg Institut and Institute for Advanced Simulation, Forschungszentrum Jülich & JARA, Jülich, Germany.*
[4] *Institut fur Theoretische Physik und Astrophysik, Universität Würzburg, Würzburg, Germany.*
[5] *Faculty of Physics, University of Duisburg-Essen and CENIDE, Duisburg, Germany.*
[6] *Department of Physics and Quantum Centers in Diamond and Emerging Materials (QuCenDiEM) Group, Indian Institute of Technology Madras, Chennai, India.*

I. THEORY MODELS FOR THE SHIBA LATTICES

A. Rectangular lattice

In this section, we discuss the model for the rectangular lattice proposed in Eqs. (1) and (2) of the Methods section. As described in the main text, we construct a tight binding-model for the lowest-lying Shiba orbitals, transforming in the irreducible representation of the site symmetry group of the $1a$ Wyckoff position. The nearest-neighbour hopping along the [001] and [1$\bar{1}$0] crystallographic axes are t_x and t_y respectively. Similarly, the Rashba-spin orbit coupling strength is parametrized by λ_x and λ_y for the two crystallographic directions. The parameter for the Hund's coupling between the spin of the Cr magnetic moments and electron spin is J, and the sign in front of the interacting term alternates depending on the orientation of the adatom spin, according to the antiferromagnetic pattern. For convenience, we introduce the anisotropy parameter $\alpha \in [0, \pi/2]$, which interpolates between the two fully anisotropic limits ($\alpha = 0, \pi/2$) and the square lattice limit ($\alpha = \pi/4$)

$$t_x = t\,\cos\alpha, \quad t_y = t\,\sin\alpha, \quad \lambda_x = \lambda\,\cos\alpha, \quad \lambda_y = \lambda\,\sin\alpha. \tag{S1}$$

Note that for the experimental termination A, with [001] and [1$\bar{1}$0] corresponding to x and y directions, the anisotropy lies within the range $0 < \alpha < \pi/2$. In momentum space, the normal state Bloch matrix $H_{\rm n}(\boldsymbol{k})$, in the basis corresponding to $\Psi_{{\rm n}\boldsymbol{k}} = (\hat{c}_{\boldsymbol{k}\uparrow 1}, \hat{c}_{\boldsymbol{k}\downarrow 1}, \hat{c}_{\boldsymbol{k}\uparrow 2}, \hat{c}_{\boldsymbol{k}\downarrow 2}, \hat{c}_{\boldsymbol{k}\uparrow 3}, \hat{c}_{\boldsymbol{k}\downarrow 3}, \hat{c}_{\boldsymbol{k}\uparrow 4}, \hat{c}_{\boldsymbol{k}\downarrow 4})$, reads

$$H_{\rm n}(\boldsymbol{k}) = \begin{pmatrix} J\sigma^z - \mu\sigma^0 & h_x(k_x) & h_y(k_y) & 0 \\ h_x^\dagger(k_x) & -J\sigma^z - \mu\sigma^0 & 0 & h_y(k_y) \\ h_y^\dagger(k_y) & 0 & -J\sigma^z - \mu\sigma^0 & h_x(k_x) \\ 0 & h_y^\dagger(k_y) & h_x^\dagger(k_x) & J\sigma^z - \mu\sigma^0 \end{pmatrix}, \tag{S2}$$

where we defined the hopping matrices as

$$h_x(k_x) = t_x(1 + e^{{\rm i}k_x})\sigma^0 - {\rm i}\lambda_x\sigma^y(1 - e^{{\rm i}k_x}) \quad \text{and} \quad h_y(k_y) = t_y(1 + e^{{\rm i}k_y})\sigma^0 + {\rm i}\lambda_y\sigma^x(1 - e^{{\rm i}k_y}). \tag{S3}$$

With the assumption of J being the dominant energy scale, the normal state band structure splits into two sets of bands, separated by an energy gap of $\sim 2J$. The Bogoliubov de Gennes Hamiltonian, with s-wave superconducting pairing induced from the bulk, is

$$H(\boldsymbol{k}) = \begin{pmatrix} H_{\rm n}(\boldsymbol{k}) & \hat{\Delta} \\ \hat{\Delta}^\dagger & -H_{\rm n}^*(-\boldsymbol{k}) \end{pmatrix}, \quad \hat{\Delta} = \Delta \begin{pmatrix} {\rm i}\sigma^y & 0 & 0 & 0 \\ 0 & {\rm i}\sigma^y & 0 & 0 \\ 0 & 0 & {\rm i}\sigma^y & 0 \\ 0 & 0 & 0 & {\rm i}\sigma^y \end{pmatrix}, \tag{S4}$$

with basis spinor $\Psi_{\boldsymbol{k}} = (\hat{c}_{\boldsymbol{k}\uparrow 1}, \hat{c}_{\boldsymbol{k}\downarrow 1}, ..., \hat{c}_{\boldsymbol{k}\uparrow 4}, \hat{c}_{\boldsymbol{k}\downarrow 4}, \hat{c}^\dagger_{-\boldsymbol{k}\uparrow 1}, \hat{c}^\dagger_{-\boldsymbol{k}\downarrow 1}, ..., \hat{c}^\dagger_{-\boldsymbol{k}\uparrow 4}, \hat{c}^\dagger_{-\boldsymbol{k}\downarrow 4})$ and Δ the superconducting pairing amplitude.

The phase diagram as a function of the chemical potential μ and α is shown in Figure S1a and consists of four phases, either gapped or gapless. While the outer regions correspond to a trivial gapped phase, between the two critical values $\mu_{1,2}$ there are two gapless phases (1 and 3), where four gapless Dirac cones are present, and two gapped

topological phases (2_x and 2_x). The phase boundaries between the trivial gapped phase -unlabeled- and the two gapless phases, labeled by 1 and 3, are described by the α-independent values

$$|\mu_{1,2}| = \sqrt{(J \pm 2\lambda)^2 - \Delta^2} \tag{S5}$$

with either positive or negative μ. The symmetry under $\lambda \to -\lambda$ originates from the spinless time-reversal symmetry of the Hamiltonian

$$H(-k_x, -k_y, -\lambda_x, \lambda_y) = H(k_x, k_y, \lambda_x, \lambda_y)^*. \tag{S6}$$

The separation line between phases 3 and 2_x corresponds to

$$\pm\,\mu_c = \sqrt{J^2 - \Delta^2 - 4\lambda^2 \cos(2\beta) + \mathrm{sign}(\beta) 4J\lambda\sqrt{-\cos(2\beta)}}, \quad \beta = \pm\alpha \quad \alpha \in \left[\frac{\pi}{4}, \frac{\pi}{2}\right). \tag{S7}$$

The gap closes at momentum $\boldsymbol{k} = (-k, k)$, at the value of k that solves the equation $\cos(k) = \cot(\alpha)$. Similarly, to find phase boundaries between phases 3 and 2_y, it is sufficient to replace the values of β with $\beta = \pi/2 - \alpha,\ -\pi/2 - \alpha$ in Eq. (S7), and the gap closes at two points lying on the line $\boldsymbol{k} = (k, k)$.

The rectangular lattice structure, with the assumption of antiferromagnetic ordering of the adatom spins, is characterized by two mirror operations $M_{x/y}$, which composed with time reversal symmetry lead to two spatio-temporal symmetries of the system, $\widetilde{M}_{x/y}$, as described in the main text. In the basis of the normal state Hamiltonian, the unitary part of these composite symmetries can be written as

$$\widetilde{M}_{y,\mathrm{n}}(k_y) = \begin{pmatrix} \mathrm{i}\sigma^y & 0 & 0 & 0 \\ 0 & \mathrm{i}\sigma^y & 0 & 0 \\ 0 & 0 & \mathrm{i}\sigma^y e^{-\mathrm{i}k_y} & 0 \\ 0 & 0 & 0 & \mathrm{i}\sigma^y e^{-\mathrm{i}k_y} \end{pmatrix}, \qquad \widetilde{M}_{x,\mathrm{n}}(k_x) = \begin{pmatrix} \sigma^0 & 0 & 0 & 0 \\ 0 & \sigma^0 e^{-\mathrm{i}k_x} & 0 & 0 \\ 0 & 0 & \sigma^0 & 0 \\ 0 & 0 & 0 & \sigma^0 e^{-\mathrm{i}k_x} \end{pmatrix}. \tag{S8}$$

In Nambu space, the latter two operations and particle-hole symmetry become

$$\widetilde{M}_x(k_x) = \begin{pmatrix} \widetilde{M}_{x,\mathrm{n}}(k_x) & 0 \\ 0 & \widetilde{M}^*_{x,\mathrm{n}}(-k_x) \end{pmatrix}, \qquad \widetilde{M}_x(k_x) H(k_x, k_y)^* \widetilde{M}_x(k_x)^{-1} = H(k_x, -k_y) \tag{S9}$$

$$\widetilde{M}_y(k_y) = \begin{pmatrix} \widetilde{M}_{y,\mathrm{n}}(k_y) & 0 \\ 0 & \widetilde{M}^*_{y,\mathrm{n}}(-k_y) \end{pmatrix}, \qquad \widetilde{M}_y(k_y) H(k_x, k_y)^* \widetilde{M}_y(k_y)^{-1} = H(-k_x, k_y) \tag{S10}$$

$$\mathcal{P} = \begin{pmatrix} 0 & \mathbb{1}_{8\times 8} \\ \mathbb{1}_{8\times 8} & 0 \end{pmatrix}, \qquad \mathcal{P} H(k_x, k_y)^* \mathcal{P}^{-1} = -H(-k_x, -k_y). \tag{S11}$$

The combination of either of the $\widetilde{M}_{x/y}$ with particle-hole symmetry defines an effective chiral symmetry $\widetilde{\mathcal{C}}_{x/y}$

$$\widetilde{\mathcal{C}}_{x/y} = \mathcal{P}\widetilde{M}_{x/y}, \qquad \widetilde{\mathcal{C}}_x H(k_x, k_y) \widetilde{\mathcal{C}}_x^{-1} = -H(-k_x, k_y), \quad \widetilde{\mathcal{C}}_y H(k_x, k_y) \widetilde{\mathcal{C}}_y^{-1} = -H(k_x, -k_y). \tag{S12}$$

As discussed in the Methods section, the Hamiltonian can be written in the basis of the operator $\widetilde{\mathcal{C}}_{x/y}$, where it assumes the chiral form of Eq. (3). This in turns allows to compute the chiral winding numbers ν_{x,k_x} and ν_{y,k_y} introduced in Eq. (4) in the Methods section.

Note that the unit cell choice depicted in Figure 4a can be replaced in principle by a two-atom unit cell, as in Figure S1c. This naturally leads to the modeling of the A_2 experimental termination. The Brillouin zone defined by this choice is shown in the upper panel of Figure S1c. The particle-hole invariant paths belong to the D class of the tenfold way, and the calculation of the Wilson loop along the paths gives a non-trivial topological invariant $\nu = 1$ along any of the lines and in both phases 2_x and 2_y. The Wilson loop is computed as [21]

$$W_{m,n}[l] = \overline{\exp}\left(\mathrm{i}\int d\boldsymbol{l} \cdot \langle u_m(\boldsymbol{k})|\, \boldsymbol{\nabla}_k\, |u_n(\boldsymbol{k})\rangle\right), \tag{S13}$$

where the line over the exponent indicates the path ordering operation, $u_m(\boldsymbol{k})$ are Bloch eigenstates and l is the path in momentum space. The bands considered, labeled by the indexes m, n, are the two bands lying closest to zero energy. The D class invariant is obtained as $\nu_{\mathrm{D}}[l] = \mathrm{Arg}(\mathrm{Tr}(W[l]))/\pi$. The non-trivial value of ν_{D} results into zero-energy modes at $k_a = 0, \pi$, visible in the ribbon spectra of Figure S1d, and analogous ones appear at $k_b = 0, \pi$ in the ribbon spectra with momentum k_b. The OBC termination that naturally arises from opening the boundaries

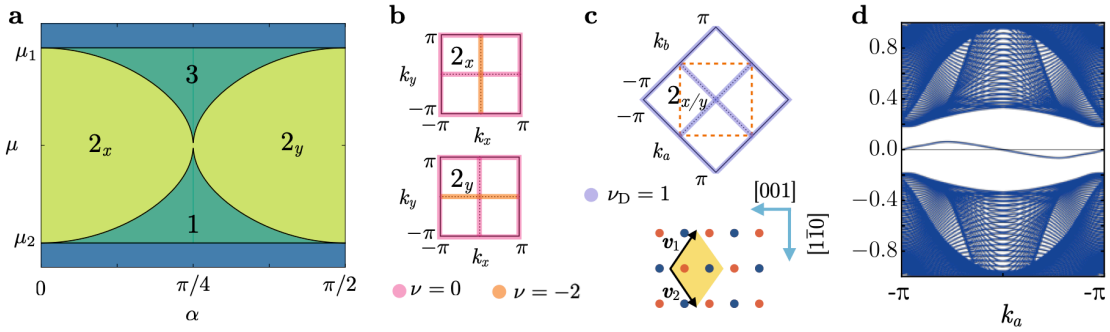

FIG. S1. **a** Phase diagram for the tight binding model of Eq. (2), corresponding to the rectangular lattice. The phase filled in blue is a trivial gapped phase, phases 1 and 3 are gapless, and phases 2_x and 2_y are gapped topological phases. **b** Brillouin zone of the rectangular lattice in phase 2_x and 2_y. Colored lines indicate paths in k-space where the BDI chiral topological invariant is well-defined, and the value of the invariant ($\nu = 0$, $\nu = 2$) is distinguished by the color, as listed in the legend. **c** Brillouin zone obtained for the alternative choice of unit cell (shown in the lower **c** panel). The lines marked in purple are those along which the superconductor belongs to the D class of the tenfold way. There, the D class topological invariant ν_D is well-defined, and the value $\nu_D = 1$ holds in both the 2_x and 2_y phases. The dashed orange square marks the folded Brillouin zone, corresponding to the one of **b**, with the choice of unit cell considered in the main text. **d** Ribbon spectrum in phase 2_y along momentum k_a, the reciprocal momentum vector of the lattice vector $\boldsymbol{v}_1$ shown in the lower panel **d**

along the directions defined by k_a and k_b has zero-energy topological edge modes along each of the four edges, in both the 2_x and 2_y phases, see Figure S2a.

For the numerical evaluation of the model, irrespective of the choice of unit cell, we choose the parameters $J = 17$ meV, $\Delta = 1.5$ meV, $\alpha = 0.4$, $t = 4$ meV, $\lambda = 1.1$ meV, $\mu = 17.2$ meV and thermal broadening $\varepsilon = 0.16$ meV. These values are kept the same for every numerical plot referring to the rectangular lattice, including those in the main text.

B. Higher order topological superconductor in the rectangular lattice

Starting from the knowledge of the crystalline symmetry protected topological nature of phases 2_x and 2_y, we can design a termination where higher order topological modes appear. In the geometry corresponding to the lattice realization A_1, also reproduced theoretically in Figure 4f, each point along the two $[1\bar{1}0]$ edges is left invariant under the action of the symmetry $\widetilde{M}_y$. To construct a higher order topological mode, we bend the straight edges to form an angle, such that the only boundary point left invariant under the symmetry remains a single corner, one for each one of the edges. This leads to higher order topological Majorana modes, localized at the corners and appearing at zero energy. With an appropriate choice of angle, the edge modes visible in the LDOS of Figure 4g are lifted from zero energy, and the emerging corner modes become separated by a gap from the remaining excited states. The predicted energy spectrum for this geometry is displayed in Figure S2a, while the electronic part of the LDOS of the two corner modes is shown in Figure S2d, where the enhanced LDOS at the corners is visible.

C. Rhombic lattice

We model the rhombic lattice for the B terminations with the tight-binding superconducting model introduced in Eq. (5) in the Method section. As for the rectangular lattice, here we consider nearest-neighbor hopping, spin-orbit coupling, and Hund's coupling between electron spin and adatom magnetic moments. In addition, we also include next-to-nearest hopping and spin-orbit coupling terms, to ensure that there are no additional artificial symmetries left in the theoretical model. In the momentum-space basis corresponding to $\Psi_{n\boldsymbol{k}} = (\hat{c}_{\boldsymbol{k}\uparrow 1}, \hat{c}_{\boldsymbol{k}\downarrow 1}, \hat{c}_{\boldsymbol{k}\uparrow 2}, \hat{c}_{\boldsymbol{k}\downarrow 2})$, the normal state Bloch Hamiltonian reads

$$H_n(\boldsymbol{k}) = \begin{pmatrix} J\sigma^z - \mu\sigma^0 + h_{nn}(k_x,k_y) & h_t(k_x,k_y) + h_{soc}(k_x,k_y) \\ h_t^\dagger(k_x,k_y) + h_{soc}^\dagger(k_x,k_y) & -J\sigma^z - \mu\sigma^0 + h_{nn}(k_x,k_y) \end{pmatrix} \tag{S14a}$$

where we defined the hopping and spin orbit coupling matrix elements as follows

$$h_t(k_x,k_y) = \sigma^0 t(1 + e^{ik_x} + e^{ik_y} + e^{i(k_x+k_y)}) \tag{S14b}$$

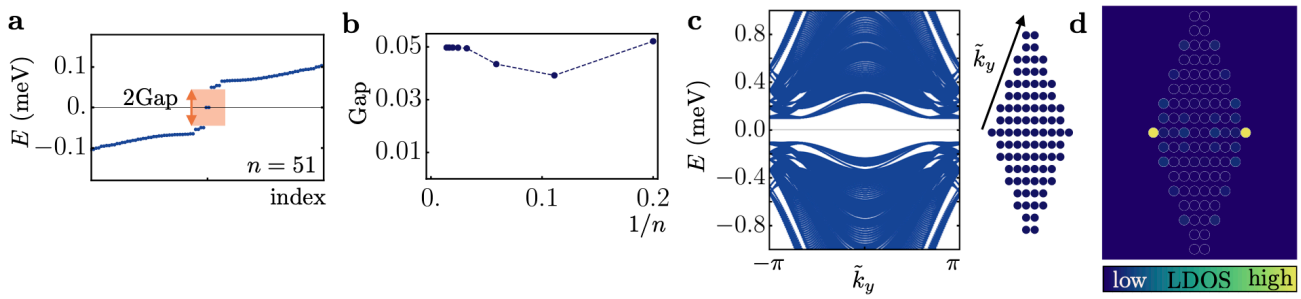

FIG. S2. **Higher order topological superconductor with corner mode a** Open boundary conditions spectrum for a termination of the A_3 type, with $n = 51$. **b** Scaling of the gap between the two zero corner modes and the remaining edge and bulk states for A_3-like terminations as a function of the inverse size $1/n$. **c** Ribbon calculation for the termination A_3, with periodic direction $\tilde{k}_y$, marked in the scheme on the right. From the ribbon spectrum one sees that the mirror symmetry breaking edge is gapped. **d** Electronic part of the LDOS for the two states closest to zero energy for the termination corresponding to the experimental termination A_3. An increased LDOS at the two corners preserving $\widetilde{M}_x$ is visible.

$$h_{\rm soc}(k_x,k_y) = -\mathrm{i}[(d_x\sigma^y - d_y\sigma^x) - (\sigma^y d_x - d_y\sigma^x)e^{\mathrm{i}k_x} + (\sigma^y d_x + d_y\sigma^x)e^{\mathrm{i}k_y} + (-\sigma^y d_x + d_y\sigma^x)e^{\mathrm{i}(k_x+k_y)}] \tag{S14c}$$

$$h_{\rm nn}(k_x,k_y) = 2(t_x\cos k_x + t_y\cos k_y)\sigma^0 + (-\lambda_x\sin k_x\sigma^y + \lambda_y\sin k_y\sigma^x). \tag{S14d}$$

With s-wave superconducting pairing, the Bogoliubov de Gennes Hamiltonian in Nambu space becomes

$$H(\boldsymbol{k}) = \begin{pmatrix} H_{\rm n}(\boldsymbol{k}) & \hat{\Delta} \\ \hat{\Delta}^\dagger & -H_{\rm n}^*(-\boldsymbol{k}) \end{pmatrix}, \quad \hat{\Delta} = \Delta \begin{pmatrix} \mathrm{i}\sigma^y & 0 \\ 0 & \mathrm{i}\sigma^y \end{pmatrix}, \tag{S15}$$

where we adopted as basis spinor $\Psi_{\boldsymbol{k}} = (\hat{c}_{\boldsymbol{k}\uparrow 1}, \hat{c}_{\boldsymbol{k}\downarrow 1}, \hat{c}_{\boldsymbol{k}\uparrow 2}, \hat{c}_{\boldsymbol{k}\downarrow 2}, \hat{c}^\dagger_{-\boldsymbol{k},1,\uparrow}, \hat{c}^\dagger_{-\boldsymbol{k}\downarrow 1}, \hat{c}^\dagger_{-\boldsymbol{k}\uparrow 2}, \hat{c}^\dagger_{-\boldsymbol{k}\downarrow 2})$.

In the thermodynamic limit of this model, the bulk is either trivially gapped or has gapless nodal points that are symmetry protected by the crystal symmetries. The gapped phase is topologically trivial, and it occurs for values of the chemical potential μ far from the value of J, the Hund's coupling term which determines the splitting between sets of bands of the normal state Hamiltonian. The gap closings occur either at the high symmetry point $\boldsymbol{k} = (0,\pi)$, for the value of the chemical potential

$$\mu^c_{(0,\pi)} = \pm d_y \pm \sqrt{J^2 - \Delta^2} + 2(t_x - t_y) \tag{S16}$$

or at the high symmetry momentum $\boldsymbol{k} = (\pi, 0)$, for critical chemical potential

$$\mu^c_{(\pi,0)} = \pm d_x \pm \sqrt{J^2 - \Delta^2} - 2(t_x - t_y). \tag{S17}$$

As for the rectangular lattice, we describe the parameters for the [001] and [1$\bar{1}$0] crystallographic axes in terms of the anisotropy parameter α. More explicitly

$$d_x = d\cos\alpha,\ d_y = d\sin\alpha, \quad t_x = t_{\rm nn}\cos\alpha,\ t_y = t_{\rm nn}\sin\alpha, \quad \lambda_x = \lambda\cos\alpha,\ \lambda_y = \lambda\sin\alpha, \tag{S18}$$

where $t_{\rm nn}$ and λ describe the next-to-nearest neighbor hopping and spin-orbit coupling amplitudes respectively. The phase diagram as a function of chemical potential μ and anisotropy α, obtained using Eqs. (S17), (S16) and (S18), is shown in Figure S3.

To see why the gapless nodal features are protected by the crystalline symmetries of the lattice, we consider the latter and their action in momentum space. In the basis of the normal state Hamiltonian, the glide mirrors M_x and M_y are

$$M_{x,\rm n}(k_y) = \begin{pmatrix} 0 & \mathrm{i}\sigma^x e^{ik_y} \\ \mathrm{i}\sigma^x & 0 \end{pmatrix} \qquad M_{y,\rm n}(k_x) = \begin{pmatrix} 0 & \mathrm{i}\sigma^y e^{ik_x} \\ \mathrm{i}\sigma^y & 0 \end{pmatrix} \tag{S19}$$

and in Nambu space with spinor $\Psi_{\boldsymbol{k}} = (\hat{c}_{\boldsymbol{k}\uparrow 1}, \hat{c}_{\boldsymbol{k}\downarrow 1}, \hat{c}_{\boldsymbol{k}\uparrow 2}, \hat{c}_{\boldsymbol{k}\downarrow 2}, \hat{c}^\dagger_{-\boldsymbol{k},1,\uparrow}, \hat{c}^\dagger_{-\boldsymbol{k}\downarrow 1}, \hat{c}^\dagger_{-\boldsymbol{k}\uparrow 2}, \hat{c}^\dagger_{-\boldsymbol{k}\downarrow 2})$, glide mirrors operations and particle-hole symmetry take the form

$$M_{x/y}(k_{y/x}) = \begin{pmatrix} M_{x/y,\rm n}(k_{y/x}) & 0 \\ 0 & M^*_{x/y,\rm n}(-k_{y/x}) \end{pmatrix}, \quad \mathcal{P} = \begin{pmatrix} 0 & \mathbb{1} \\ \mathbb{1} & 0 \end{pmatrix} \tag{S20}$$

Starting from these expressions for the glide mirrors, one can see that two eigenstates that are paired by the superconducting coupling are characterized by opposite M_x eigenvalue at $k_x = \pi$, and therefore cannot hybridize and open a gap. Likewise, the eigenstates at $k_y = \pi$ have opposite M_y eigenvalues. It is useful to first derive the commutation relations between glide mirror symmetries at momenta $k_x = 0, \pi$, which read

$$\begin{aligned} M_x(0,-k_y)M_y(0,k_y) &= -e^{-\mathrm{i}k_y} M_y(0,k_y)M_x(0,k_y) \\ M_x(\pi,-k_y)M_y(\pi,k_y) &= e^{-\mathrm{i}k_y} M_y(\pi,k_y)M_x(\pi,k_y) \\ M_y(-k_x,0)M_x(k_x,0) &= -e^{-\mathrm{i}k_x} M_x(k_x,0)M_y(k_x,0) \\ M_y(-k_x,\pi)M_x(k_x,\pi) &= e^{-\mathrm{i}k_x} M_x(k_x,\pi)M_y(k_x,\pi). \end{aligned} \tag{S21}$$

Let us consider an eigenstate of the glide mirror symmetry M_x at $k_x = \pi$, with

$$M_x(\pi,k_y)\,|\psi^{\pm}(\pi,k_y)\rangle = \pm\mathrm{i}e^{\mathrm{i}\frac{k_y}{2}}\,|\psi^{\pm}(\pi,k_y)\rangle\,. \tag{S22}$$

The state that pairs with $|\psi^{\pm}(\pi,k_y)\rangle$ can be obtained by applying particle-hole symmetry and then M_y to the latter

$$|\widetilde{\psi}^{\pm}(\pi,k_y)\rangle = M_y(\pi,-k_y)\mathcal{P}\,|\psi^{\pm}(\pi,k_y)\rangle\,. \tag{S23}$$

For the state in (S23), we compute the transformation properties under the action of M_x, and find

$$\begin{aligned} M_x(\pi,k_y)\,|\widetilde{\psi}^{\pm}(\pi,k_y)\rangle &= M_x(\pi,k_y)M_y(\pi,-k_y)\mathcal{P}\,|\psi^{\pm}(\pi,k_y)\rangle \\ &= \mathcal{P}M_x(\pi,-k_y)M_y(\pi,k_y)\,|\psi^{\pm}(\pi,k_y)\rangle \\ &= \mathcal{P}M_y(\pi,k_y)M_x(\pi,k_y)e^{\mathrm{i}k_y}\,|\psi^{\pm}(\pi,k_y)\rangle \\ &= \mathcal{P}M_y(\pi,k_y)(\pm\mathrm{i}e^{\mathrm{i}\frac{k_y}{2}})e^{-\mathrm{i}k_y}\,|\psi^{\pm}(\pi,k_y)\rangle \\ &= \mp\mathrm{i}e^{\mathrm{i}\frac{k_y}{2}} M_y(\pi,k_y)\mathcal{P}\,|\psi^{\pm}(\pi,k_y)\rangle = \mp\mathrm{i}e^{\mathrm{i}\frac{k_y}{2}}\,|\widetilde{\psi}^{\pm}(\pi,k_y)\rangle\,. \end{aligned} \tag{S24}$$

Eq. (S24) implies that the two eigenstates connected by the superconducting pairing remain degenerate, as they carry opposite M_x eigenvalue. Following the same procedure, one can show that the two eigenstates of M_x that pair at $k_x = 0$ have the same mirror eigenvalue, and therefore the degeneracy between the two eigenstates can be lifted, in accordance with the absence of gapless points along the high symmetry line $(0, k_y)$. With the same arguments, one can see that eigenstates paired by superconductivity at $k_y = \pi$ carry opposite M_y eigenvalue, while they have the same eigenvalue at $k_y = 0$.

The composition of time reversal symmetry $\mathcal{T}$ and standard mirror symmetries $M'_{x/y}$ leads to an effective time reversal symmetry $\widetilde{M}$ with $\widetilde{M}^2 = (\mathcal{T}M'_{x/y})^2 = +\mathbb{1}$. Therefore, chiral symmetry $\mathcal{C} = \widetilde{M}\mathcal{P}$ is well defined and we can compute the chiral topological invariant of class BDI for any gapless particle-hole invariant path, see Figure S3b,c.

In the numerical plots appearing throughout the Supplementary Information and the main text, we used the parameters $J = 17$ meV, $\Delta = 1.5$ meV, $t = 4.0$ meV, $\mu = 20$ meV, $\alpha = 0.5$, $d = 1$ meV, $t_{\mathrm{nn}} = 2$ meV, $\lambda = 0.1$ meV and thermal broadening $\varepsilon = 0.16$ meV, used in the calculation of the LDOS maps at zero energy.

D. Importance of spin-orbit coupling

As an additional comment on the discussions presented in Sec. I A and Sec. I C, we shortly consider the case of no spin-orbit coupling in the models for the Shiba lattices. When spin-orbit coupling is absent, the the two type of lattices, both rectangular and rhombic, are gapped and have no non-trivial topological features. Figure S4 shows the Fermi surface and the ribbon spectra corresponding to the ones shown in Figure 4, with all the spin-orbit coupling strength parameters set to zero.

The prediction of a gapless bulk for the terminations A and B, in the absence of spin-orbit coupling, is in contrast with the experimental observations. In fact, Figure 2 hints at a non-zero LDOS close to zero bias in all the measured terminations, either for the the edges of the structures or in their bulk.

E. Discussion of adatom spins with in-plane component

In this section, we discuss the consequences of relaxing the assumption of adatom spins aligned along the z-direction. Instead, we admit an in-plane component of the spin. Based on the experimental measurements on 1D chains and on

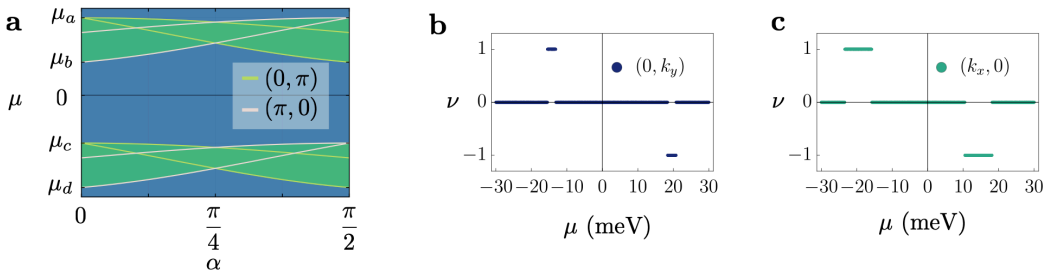

FIG. S3. **a** Phase diagram for the rhombic lattice as a function of of chemical potential μ and anisotropy parameter α. Regions shaded in blue correspond to gapped spectrum of the Bogoliubov de Gennes Hamiltonian, while regions colored in green have gapless points along lines with either $k_x = \pi$ or $k_y = \pi$. The gap closings occur at the high symmetry points $\boldsymbol{k} = (0, \pi)$ (black lines) or $\boldsymbol{k} = (\pi, 0)$ (yellow lines). Here, μ_{a-d} only mark the values at the phase boundaries assumed by the critical chemical potential introduced in Eqs. (S17), (S16) at $\alpha = 0$. **b**,**c**: Chiral winding number of the Bogoliubov de Gennes Hamiltonian in case B for a cut along the phase diagram **a** with constant $\alpha = 0.5$. The paths considered are **b** $\boldsymbol{k} = (0, k)$ and **c** $\boldsymbol{k} = (k, 0)$ for $k \in [-\pi, \pi)$.

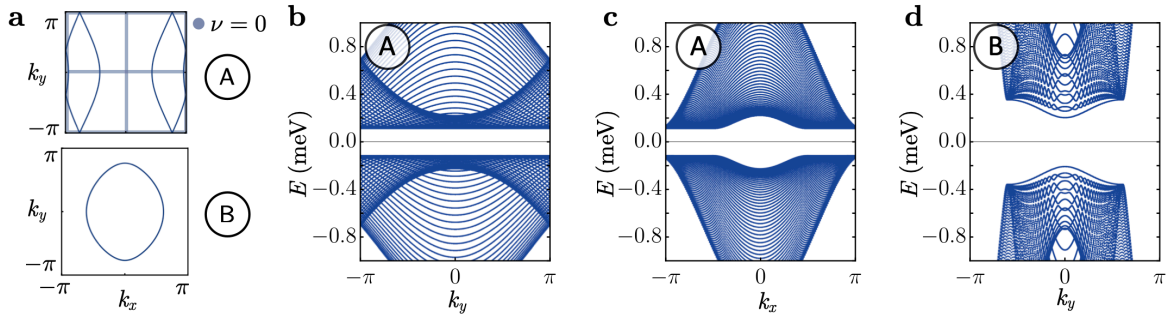

FIG. S4. **Absence of spin-orbit coupling:** **a** Normal state Fermi surface for the rectangular (upper figure) and rhombic (lower figure) lattices. The high symmetry lines in the Brillouin zone of the rectangular lattice are colored according to the value of the topological invariant, which is everywhere trivial. **b-d**: Ribbon spectra for the rectangular lattice with open boundary conditions along **b** x and **c** y, and ribbon spectra for the rhombic lattice **d** with open boundary conditions along x.

the DFT calculations discussed in the main text, we assume that the antiferromagnetic ordering is maintained. For this, we parametrize the adatom spins by

$$\pm\, \boldsymbol{S} = \pm S(\boldsymbol{e}_z \cos\theta + \boldsymbol{e}_x \sin\theta\cos\phi + \boldsymbol{e}_y \sin\theta\sin\phi) \tag{S25}$$

with the usual definition of spherical angles $\phi \in [0, 2\pi)$ and $\theta \in [0, \pi)$, and where the alternating sign should reproduce the antiferromagnetic pattern. Figure S5 shows the scheme for the magnetic ordering of the two lattices considered.

In practice, this amounts to replacing the terms $\pm J\sigma^z$ in the Hamiltonians (S2) and (S14a) by

$$\pm\, J\sigma^z \to \pm J(\sigma^z \cos\theta + \sigma^x \sin\theta\cos\phi + \sigma^y \sin\theta\sin\phi). \tag{S26}$$

In the following, we denote Hamiltonians with the replacement (S26) by $H_{S,\mathrm{n}}(\boldsymbol{k})$ and $H_S(\boldsymbol{k})$ for the normal state and Bogoliubov de Gennes Hamiltonians respectively.

a. Rectangular lattice First, we focus on the case of the rectangular lattice, relevant for the termination A. For a small tilting of the spins, i.e. $\theta \ll 1$, the phase diagram shown in Figure S1a remains qualitatively unchanged, apart from a renormalization of the boundaries between different phases. With the replacement (S26), the mirror operations $M_{x/y}$ and the glide mirror operations combined with time reversal symmetry $\widetilde{M}_{x/y}$ are no longer symmetries of the lattice. Nevertheless, there are two crystalline symmetries left, which are defined by the composition of time reversal symmetry and half a lattice translation in either the x or y direction, see Figure S5a. These two operations, denoted by $\widetilde{T}_{x/y} = \mathcal{T} T_{\boldsymbol{a}_{x/y}/2}$, define an effective time reversal symmetry in the crystal. In this case $\widetilde{T}_x^2 = -e^{\mathrm{i}k_x}\mathbb{1}$ and $\widetilde{T}_y^2 = -e^{\mathrm{i}k_y}\mathbb{1}$,

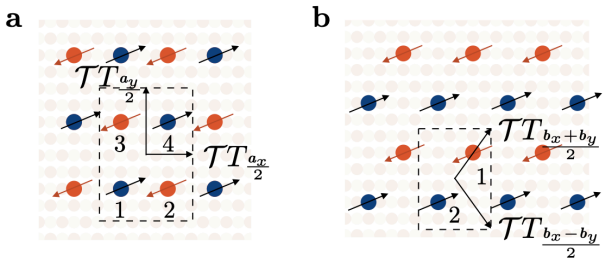

FIG. S5. Antiferromagnetic ordering of the spins in **a** the rectangular and **b** rhombic lattice. The choice of unit cell is highlighted by the dashed rectangles, and the half-lattice traslations discussed in the text are marked by black arrows. Here colored dots indicate the z component of the spins either up (red) or down (blue), and the arrows indicate the in-plane projection of the spins. Red (blue) sites correspond to spins with $+\boldsymbol{S}$ ($-\boldsymbol{S}$) in Eq. (S25).

and the unitary part of these operations acts on the normal state Hamiltonian as

$$\widetilde{T}_{x,\mathrm{n}}(k_x) = \begin{pmatrix} 0 & \mathrm{i}\sigma^y & 0 & 0 \\ \mathrm{i}\sigma^y e^{\mathrm{i}k_x} & 0 & 0 & 0 \\ 0 & 0 & 0 & \mathrm{i}\sigma^y \\ 0 & 0 & \mathrm{i}\sigma^y e^{\mathrm{i}k_x} & 0 \end{pmatrix}, \qquad \widetilde{T}_{y,\mathrm{n}}(k_y) = \begin{pmatrix} 0 & 0 & \mathrm{i}\sigma^y e^{-\mathrm{i}k_y} & 0 \\ 0 & 0 & 0 & \mathrm{i}\sigma^y e^{-\mathrm{i}k_y} \\ \mathrm{i}\sigma^y & 0 & 0 & 0 \\ 0 & \mathrm{i}\sigma^y & 0 & 0 \end{pmatrix} \tag{S27}$$

The extension to Nambu space of the latter reads

$$\widetilde{T}_{x/y}(k_{x/y}) = \begin{pmatrix} \widetilde{T}_{x/y,\mathrm{n}}(k_{x/y}) & 0 \\ 0 & \widetilde{T}^*_{x/y,\mathrm{n}}(-k_{x/y}) \end{pmatrix}, \tag{S28}$$

and the action on the Bogoliubov de Gennes Hamiltonian is

$$\widetilde{T}_x(k_x) H_S^*(k_x,k_y) \widetilde{T}_x^{-1}(k_x) = H_S(-k_x,-k_y), \qquad \widetilde{T}_y(k_y) H_S^*(k_x,k_y) \widetilde{T}_y^{-1}(k_y) = H_S(-k_x,-k_y). \tag{S29}$$

Particle-hole symmetry is still a valid symmetry of the system, hence we can still assign the high symmetry lines in the Brillouin zone to some of the classes in the tenfold way. More precisely, the lines parametrized by $\boldsymbol{k} = (0,k)$ and $\boldsymbol{k} = (k,0)$, with $k \in [0,2\pi)$, belong to the DIII class of the tenfold way, while $\boldsymbol{k} = (\pi,k)$ and $\boldsymbol{k} = (k,\pi)$, for $k \in [0,2\pi)$, belong to the BDI class. This allows to define the topological invariants $\tilde{\nu}_{x,k_x=0}, \tilde{\nu}_{y,k_y=0} \in \mathbb{Z}_2$ for the lines in class DIII and $\nu_{x,k_x=\pi}, \nu_{y,k_y=\pi} \in \mathbb{Z}$ for the lines in class BDI. The topological invariants ν and $\tilde{\nu}$ can be computed from the chiral winding number (4) and the Wilson loop (S13) respectively. From the evaluation of these invariants for a range of parameters, we obtain that ν_{x,k_x} and ν_{y,k_y} always remain trivial, irrespective of the value of the chemical potential μ, while $\tilde{\nu}_{x,k_x} = 1$ and $\tilde{\nu}_{y,k_y} = 0$ in the topological phases corresponding to 2_x and 2_y. Hence, even in the case of a generic adatom spin direction, there are two topological zero modes protected by the effective time-reversal symmetry and particle-hole symmetry, that appear along the y-edges of an open boundary termination analogous to A. These topological modes are still protected by a lattice symmetry, in particular the half-lattice translation $T_{\boldsymbol{a}_y/2}$, which is still respected at the y-boundaries of A. Therefore, this system realizes a topological crystalline insulator as long as antiferromagnetic ordering is ensured, irrespective of the direction of the adatom spins.

Although the topological boundary modes are stable when choosing (S25), the arguments for the higher order topological modes described in Sec. I B fail in the case of a generic adatom spin orientation. In fact, the condition for the realization of the corner mode at zero energy relies on the corner being invariant under the action of the mirror operation $\widetilde{M}_y$, which is no longer a symmetry of $H_S(\boldsymbol{k})$.

b. Rhombic lattice For the case of the rhombic lattice, once more the mirror operations $M_{x/y}$ and $\widetilde{M}_{x/y}$ are no longer symmetries of the lattice once a generic adatom spin orientation is considered. Under the assumption of antiferromagnetic ordering, the system retains the invariance under the combination of a half-lattice translation in each direction, $T_{(\boldsymbol{b}_x \pm \boldsymbol{b}_y)/2}$ combined with time-reversal symmetry, see Figure S5b. In the following, we only consider $T_{(\boldsymbol{b}_x+\boldsymbol{b}_y)/2}$ as the two translations are equivalent up to a global phase factor. This half-lattice translation defines an effective time-reversal symmetry $\widetilde{T} = \mathcal{T}T_{(\boldsymbol{b}_x+\boldsymbol{b}_y)/2}$. This operation can be written as

$$\widetilde{T}_{\mathrm{n}}(\boldsymbol{k}) = \begin{pmatrix} 0 & \sigma^y e^{-\mathrm{i}\frac{(k_x+k_y)}{2}} \\ \sigma^y e^{\mathrm{i}\frac{(k_x+k_y)}{2}} & 0 \end{pmatrix}, \qquad \widetilde{T}(\boldsymbol{k}) = \begin{pmatrix} \widetilde{T}_{\mathrm{n}}(\boldsymbol{k}) & 0 \\ 0 & -\widetilde{T}^*_{\mathrm{n}}(-\boldsymbol{k}) \end{pmatrix} \tag{S30}$$

and the action of the Bogoliubov de Gennes Hamiltonian is

$$\widetilde{T}(\boldsymbol{k})H_S^*(\boldsymbol{k})\widetilde{T}^{-1}(\boldsymbol{k}) = H_S(-\boldsymbol{k}). \tag{S31}$$

The combination of $\widetilde{T}$ with particle-hole symmetry $\mathcal{P}$ results in a unitary operator $U(\boldsymbol{k}) = \widetilde{T}(-\boldsymbol{k})\mathcal{P}$ that anticommutes with the Hamiltonian

$$U(\boldsymbol{k}) = \begin{pmatrix} 0 & 0 & 0 & \sigma^y e^{\mathrm{i}\frac{(k_x+k_y)}{2}} \\ 0 & 0 & \sigma^y e^{-\mathrm{i}\frac{(k_x+k_y)}{2}} & 0 \\ 0 & \sigma^y e^{\mathrm{i}\frac{(k_x+k_y)}{2}} & 0 & 0 \\ \sigma^y e^{-\mathrm{i}\frac{(k_x+k_y)}{2}} & 0 & 0 & 0 \end{pmatrix}, \quad U(\boldsymbol{k})H(\boldsymbol{k})U^{-1}(\boldsymbol{k}) = -H(\boldsymbol{k}), \tag{S32}$$

hence realizing an effective chiral symmetry. This anticommutation relation protects the nodal points, although it does not constrain them to be fixed at the high symmetry lines with $k_x = \pi$ or $k_y = \pi$, as it was the case in Sec. I C. In fact, adding a term to the Hamiltonian

$$H_S(\boldsymbol{k}) \to H_S(\boldsymbol{k}) + U(\boldsymbol{k}) \tag{S33}$$

would open a gap in the bulk energy spectrum, but would also violate the condition (S32). Hence, for a small tilting of the adatom spin direction, meaning $\theta \ll 1$ in (S25), the bulk is still gapless and has nodal points close to the high symmetry lines at $k_x = \pi$ or $k_y = \pi$, where they are pinned for adatom spins aligned along the out-of-plane direction.